The short-term seismicity of the Central Ionian Islands (Greece) studied by means of a clustering model

Ourania Mangira [1], Rodolfo Console,[2,3] Eleftheria Papadimitriou,[1] Maura Murru[2] and Vasilios Karakostas[1]

[1]*Department of Geophysics, School of Geology, Aristotle University of Thessaloniki, GR54124 Thessaloniki, Greece. E-mail: omangira@geo.auth.gr*
[2]*Istituto Nazionale di Geofisica e Vulcanologia, Via Vigna Murata 605, I-00143 Rome, Italy*
[3]*Center of Integrated Geomorphology for the Mediterranean Area, Via F. Baracca 175, I-85100 Potenza, Italy*

SUMMARY

Earthquake clustering in the area of Central Ionian Islands (Greece) is statistically modelled by means of the Epidemic Type Aftershock Sequence (ETAS) branching model, which is the most popular among the short-term earthquake clustering models. It is based upon the assumption that an earthquake is not fully related to any other one in particular, but rather to both all previous events, and the background seismicity. The close temporal proximity of the strong ($M \geq 6.0$) events in the study area offers the opportunity to retrospectively test the validity of the ETAS model through the 2014 Kefalonia doublet (M_w 6.1 and M_w 6.0) and the 2015 Lefkada aftershock sequences. The application of a physics-based earthquake simulator to the local fault system produced a simulated catalogue with time, space and magnitude behaviour in line with the observed seismicity. This catalogue is then used for the detection of short-term interactions between both strong and smaller events and the comparison between the two cases. The results show that the suggested clustering model provides reliable forecasts of the aftershock activity. Combining the ETAS model and the simulator code, though, needs to be more deeply examined since the preliminary results show some discrepancy between the estimated model parameters.

Key words: Probabilistic forecasting; Statistical methods; Statistical seismology.

1 INTRODUCTION

Earthquake interaction is investigated through the development of stochastic models that were applied in the last decades in an attempt to fill in the gap between physical and statistical models (Vere-Jones *et al.* 2005). Among them the spatiotemporal point process ones are well suited for the quantification and investigation of earthquake clustering, that is the increasing seismicity rates in relatively small temporal and spatial windows close to previous events. The Epidemic-Type Aftershock Sequence (ETAS) model, first temporal (Ogata 1988) and then spatiotemporal (Ogata 1998; Console & Murru 2001; Console *et al.* 2003) constitutes a purely statistical model for exploring earthquake clustering. The key concept upon which ETAS is formulated is that 'foreshocks', 'main shocks' and 'aftershocks' are equally considered capable to produce their own offspring and events are not independent, but related to the previous ones, according to certain weights. Since its development, the ETAS model became very popular and a starting point for short-term earthquake forecasts (Zhuang *et al.* 2004, 2008, Hainzl & Ogata 2005; Ogata & Zhuang 2006; Console *et al.* 2006a, b; Marzocchi & Lombardi 2009; 2018; Lombardi *et al.* 2010; Murru *et al.* 2014). Even though the ETAS model focuses on

describing and forecasting the aftershock activity, some researchers argue that reliable forecasts can also be provided even before the main shock of a sequence (Helmstetter & Sornette 2003; Murru *et al.* 2009; Console *et al.* 2010b; Nanjo *et al.* 2012; Ogata *et al.* 2013). Among the first researchers who performed prospective forecasts, using small earthquakes to forecast large ones, are the Keilis–Borok group, who tested the *M*8 and similar algorithms (Keilis–Borok & Kossobokov 1987, 1990; Kossobokov *et al.* 1990, 1999), and the Evison group, who tested a method of forecasting based on precursory swarms (Evison & Rhoades 1993). Later on, the relevance of small magnitude events for earthquake forecasting was also studied by Helmstetter *et al.* (2005, 2006). The international partnership Collaboratory for the Study of Earthquake Predictability (CSEP; Jordan 2006) then, initiated the development and implementation of rigorous prospective testing of several forecasting models against future observations in order to assess their performance. Observations, test procedures and metrics are agreed in advance so that full independence from the testing process is ensured. Statistical clustering models in California, New Zealand, Japan, Italy and globally, have been tested and successful results were confirmed in several experiments (Schorlemmer *et al.* 2018; Taroni do *et al.* 2018).
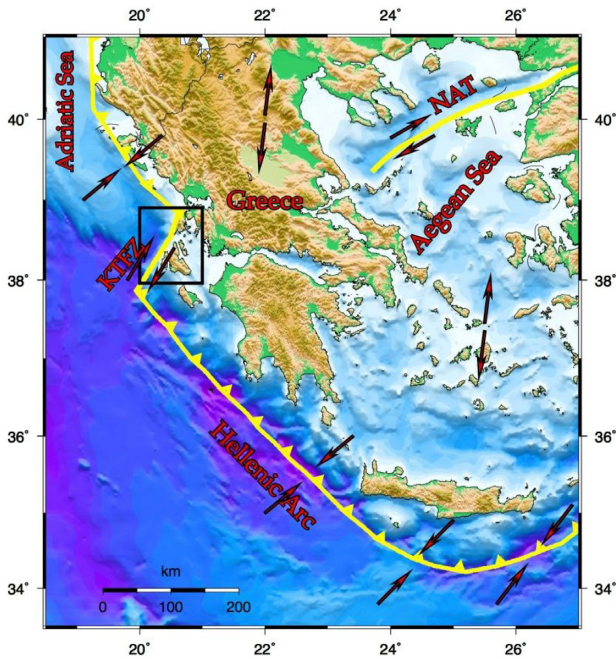
Figure 1. The main geodynamic features of the Aegean and surrounding areas shown on a relief map. The active boundaries are shown as solid lines. The arrows indicate the approximate direction of relative plate motion. The study area is denoted by the rectangle. KTFZ—Kefalonia Transform Fault Zone, NAT—North Aegean Trough.

The remarkable temporal proximity of main shocks seems suitable for the application of the ETAS model and its validation in a retrospective way in the area of Central Ionian Islands comprising Kefalonia and Lefkada Islands. High seismicity rates and frequent occurrence of strong ($M \geq 6.0$) main shocks in both the historical and instrumental eras characterize the study area, with 6 main shocks with $M \geq 6.0$ since 1983, related to different fault segments. The tight clustering of strong events indicates significant interaction on adjacent fault segments (Papadimitriou *et al.* 2017) and was explained through stress transfer by Papadimitriou (2002). For highly reliable earthquake hazard assessment, a statistical description of earthquakes for thousands of years would be ideal. Although for the investigation of short-term interactions the short duration of an instrumental catalogue may not be a problem, our aim is to investigate clustering features in a longer time window in order to find seismicity patterns and check the consistency of the model parameters. Given the shortage of earthquake catalogues in general, the physics-based earthquake simulators are engaged to generate such long earthquakes histories (Tullis *et al.* 2012b).

2 STUDY AREA

The area of Central Ionian Islands consists the most active seismic zone in the Aegean and surrounding area (Fig. 1), characterized by notable seismic moment rate ($\sim 10^{25}$ dyn cm yr^{-1}; Papazachos *et al.* 1997) and frequent occurrence of strong ($M \geq 6.0$) earthquakes. It is depicted by a rectangle in Fig. 1 (19.9°E–21.0°E, 37.8°N–38.9°N) and encompasses the Kefalonia Transform Fault Zone (KTFZ) that is recognized as an active boundary connecting the continental collision to the north with the oceanic subduction to the south, accommodating right-lateral strike slip motion (Scordilis *et al.* 1985). The spatial distribution of the most disastrous events is mainly aligned along the KTFZ, in a narrow zone running along the

western coastlines of both Islands, and the vast majority of smaller magnitude earthquakes, as evidenced in Fig. 2.

The 2003 Lefkada sequence was the motive for the installation of a dense local digital seismological network that gave the opportunity to identify secondary fault segments that were activated and capable of producing moderate to large destructive earthquakes (Karakostas *et al.* 2004; Karakostas 2008; Karakostas & Papadimitriou 2010). The most recent main shock in Lefkada with M_w 6.5 occurred on 17 November 2015, onto a fault segment, in the southern part of the Lefkada branch of KTFZ, adjacent to the 2003 event (Papadimitriou *et al.* 2017). The off-fault aftershocks distribution was apparently triggered by static stress transfer to secondary faults (Karakostas *et al.* 2004; Karakostas 2008; Karakostas & Papadimitriou 2010). Seismicity of the southern part of the aftershock zone reveals differences in the faulting style denoting a transfer zone between Lefkada and Kefalonia fault branches, consisting of small parallel extensional stepover faults (Karakostas *et al.* 2015).

The northern part of the Kefalonia branch of the KTFZ ruptured in a 2014 doublet (M_w 6.1 and M_w 6.0) with the two main events being separated temporally by 7 d and associated with adjacent fault segments, compatible with dextral shearing. The 2014 seismic sequence may be considered as the northward continuation of the 1983 sequence that occupied the southern portion of the Kefalonia branch, with partial overlap, and is located inside stress enhanced areas revealed by the application of the stress evolutionary model (Papadimitriou 2002).

Information on the main shocks ($M_w \geq 6.0$) between 1983 and 2017 and the associated five fault segments adopted in the current study, is given in Table 1. For the three 'stepover' faults, information is taken from the aftershock activity studied in Papadimitriou *et al.* (2017) as far as the faulting type and position concerned. Seismicity here does not exceed $M6.0$ and the faults' length is set equal to 7 km according to highly accurate relocation performed in previous studies (Karakostas *et al.* 2015).

3 EARTHQUAKE CLUSTERING MODELS

As it was previously mentioned, it is widely recognized that the seismicity rate increases after a large earthquake for several years (Utsu *et al.* 1995) and at distances distinctly larger than the rupture length (Kagan & Jackson 1998; Dreger & Savage 1999) revealing clustering behaviour. In the adopted ETAS model, earthquakes are considered as the realization of a point process, with each event characterized by its location–time–magnitude coordinates (x, y, t, m) while the depth coordinate (z) is ignored for simplicity and because of its formal uncertainty. Details regarding the formulation of the model used in this study are given in the Appendix A.

4 A PHYSICS-BASED EARTHQUAKE SIMULATOR

The development and application of earthquake simulators allow the generation of long synthetic earthquake catalogues that incorporate features of time, space and magnitude behaviour of the seismicity similar to those of the observations. The first proposed simulator, called Virtual California, was originally developed by Rundle (1988). It included stress accumulation and release, as well as stress interactions between the San Andreas and other adjacent faults. An updated version of Virtual California was presented in 2005 (Rundle *et al.* 2005), including fault system physics, such as the complex elastic interactions between the San Andreas and adjacent faults in
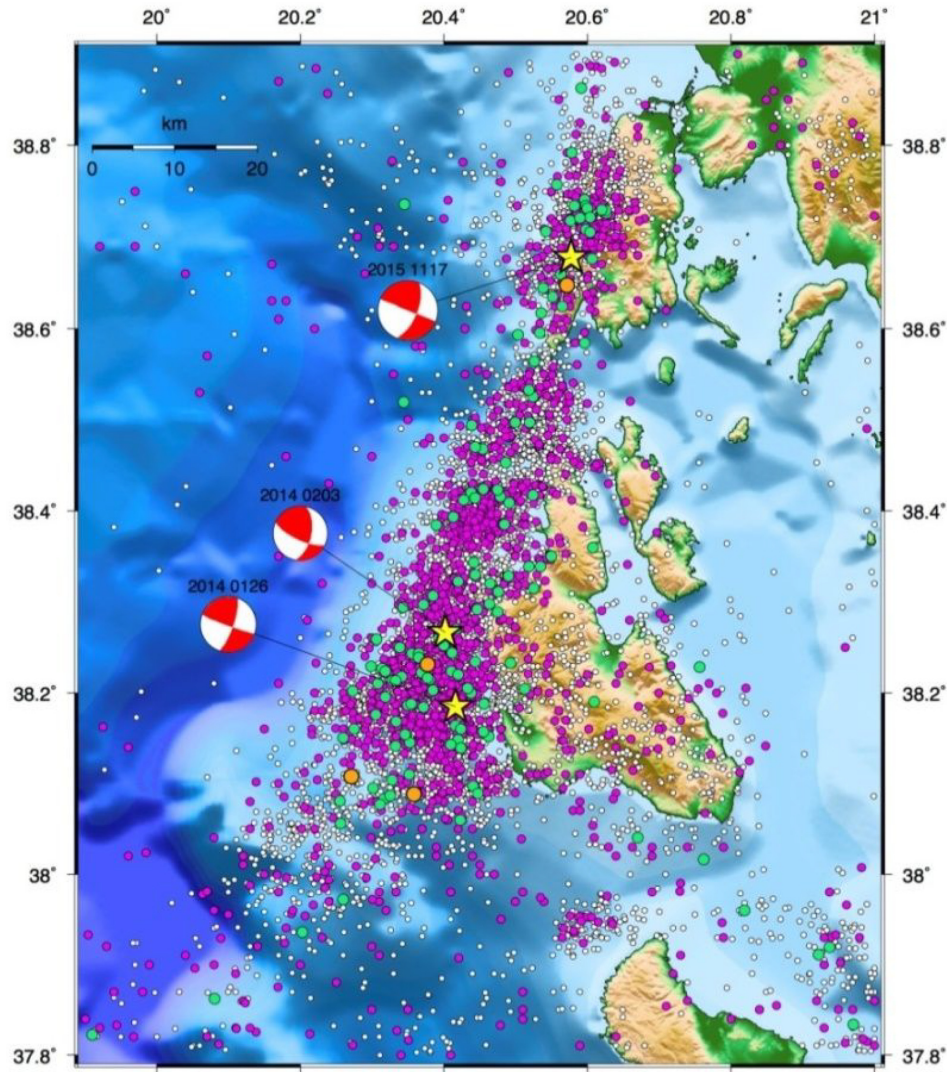
Figure 2. Spatial distribution of earthquakes with $M \geq 2.0$ that occurred from January 2008 to December 2017. Events with $2 \leq M < 3.0$, $3 \leq M < 4.0$, $4.0 \leq M < 5.0$, $5.0 \leq M < 6.0$ are depicted with white, magenta, light green and orange circles, respectively. Events with $M \geq 6.0$ are depicted with yellow stars. Fault plane solutions (http:/globalcmt.org) are also plotted as equal area Lower hemisphere projection.

Table 1. Source parameters of the characteristic events ($M_w \geq 6.0$) occurred in Central Ionian Islands between 1983 and 2017.

Origin time (GMT)		Epicentre		M_w	Mechanism			Associated fault
Date	Time	Lon (°E)	Lat (°N)		Strike (°)	Dip (°)	Rake (°)	
17/01/1983	12:41:31	38.100	20.200	7.0	40	45	168	Offshore Kefalonia
14/08/2003	05:14:55	38.744	20.539	6.2	18	60	-175	Lefkada North
26/01/2014	13:55:41	38.1990	20.4340	6.1	20	65	177	Kefalonia South
03/02/2014	03:08:44	38.2690	20.4100	6.0	12	45	154	Kefalonia North
17/11/2015	07:10:07	38.6775	20.5773	6.5	16	64	179	Lefkada South

South California, and friction laws developed with insights from laboratory experiments and field data. The simulator adopted in this study was initially developed upon the main features of earthquake simulators found in Tullis (2012), such as the long-term slip rate on seismogenic sources without taking into account rheological parameters. Although many simplifications are adopted in order to make the computations feasible and despite the fact that simulators cannot substitute the information that a reliable historical catalogue can provide, synthetic catalogues can overcome the limitations of real catalogues in terms of completeness, homogeneity and time duration, and thus they can be used for the evaluation of various models of the seismogenic processes (Wilson *et al.* 2017). A brief description is given on the algorithm of the simulator code applied here, and more details in Console *et al.* (2015, 2017, 2018).

The geometry, kinematics and average slip rate for every fault segment are prerequisite input information. The segments of the fault system are considered planar rectangular surfaces, then divided into many square cells. Since the initial status of stress is

Table 2. Aσ values used in previous publications.

Aσ (MPa)	Region	References
0.001–0.06	San Francisco, USA	Harris & Simpson (1998)
0.035 ± 0.15	Kobe, Japan	Toda *et al.* (1998)
0.02, 0.035, 0.05	San Francisco, USA	Stein (1999)
0.08, 0.09	Irpinia, Italy	Belardinelli *et al.* (1999)
0.06	Kobe, Japan	Guatteri *et al.* (2001)
0.04	Southern Kyushu, Japan	Toda & Stein (2003)
0.012	Japan	Console *et al.* (2006b)
0.0001–0.9	Umbria-Marche, Italy	Catalli *et al.* (2008)
0.0025–0.375	North Aegean, Greece	Leptokaropoulos *et al.* (2012)
0.005	Krafla rifting, Iceland	Maccaferri *et al.* (2013)
0.004	Western Corinth Gulf, Greece	Leptokaropoulos *et al.* (2016)

Table 3. Learning and testing periods in the application of the ETAS model.

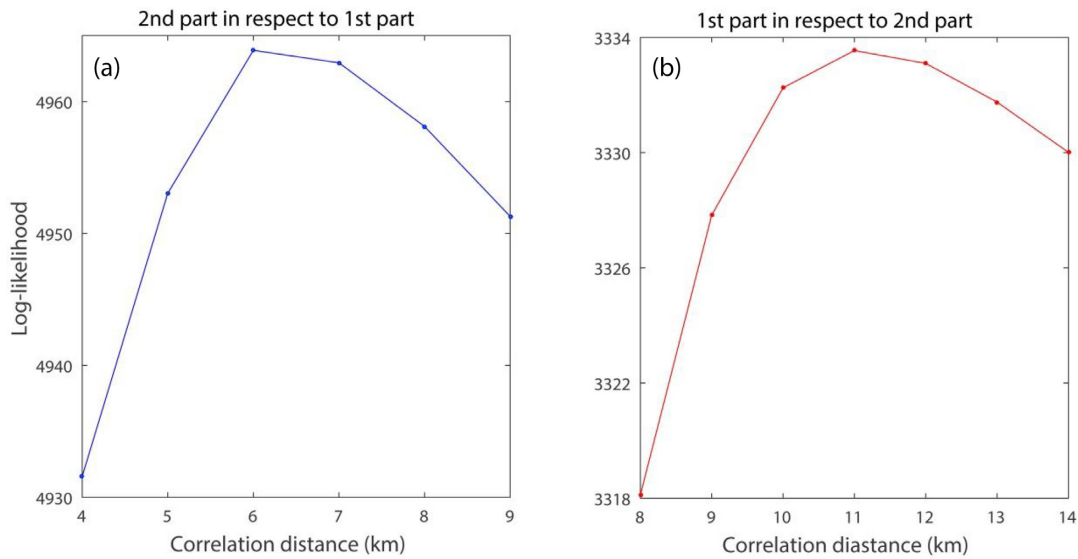| Learning period	Testing period	Main shocks included in the learning period	Main shocks included in the testing period
1 January 2008–31 October 2015	01 November 2015–31 December 2016	M_w 6.1 26 January 2014 M_w 6.0 03 February 2014	M_w 6.5 17 November 2015
1 January 2008–29 January 2014	30 January 2014–31 December 2015	M_w 6.1 26 January 2014	M_w 6.0 03 February 2014

Figure 3. (a) Plot of the likelihood of the second part of the catalogue under the time-independent Poisson model created from the first part of the catalogue, versus different values of the c parameter of the smoothing algorithm. (b) Equivalent plot for the first part of the catalogue in respect to the second.

Table 4. Values obtained for the parameters of the epidemic model in the progressive adjustment of the background seismicity.

| Parameters	1st Iteration	2nd iteration	3rd iteration	4th iteration
k (d^{p-1}), Productivity coefficient	0.14178	0.0770	0.0769	0.0769
d_0 (km), Characteristic distance in the spatial distribution	1.1263	1.4878	1.4869	1.4873
q, Exponent of the spatial distribution	1.8771	2.0409	2.0426	2.0451
c (d), Time constant in Omori law	0.0239	0.0441	0.0439	0.0441
p, Exponent in Omori law	1.1041	1.2035	1.2079	1.2089
α	0.5092	0.4502	0.4478	0.4477
f_r, Fraction of spontaneous events	0.2271	0.2636	0.2637	0.2646
ln$L$	26 107.600	26 112.680	26 113.620	**26 113.700**
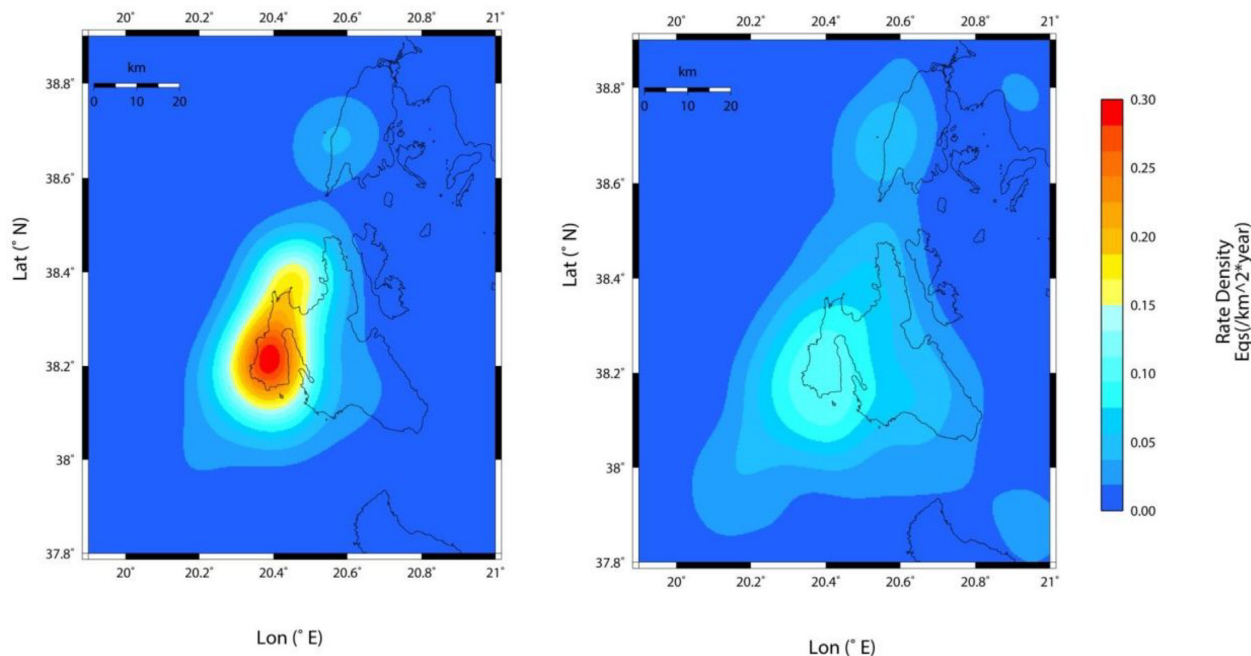
Figure 4. Smoothed distributions of the Central Ionian Islands (01 January 2008–31 October 2015) seismicity obtained by the smoothing algorithm applied to the (a) raw catalogue (b) weighted catalogue after the 4th iteration.
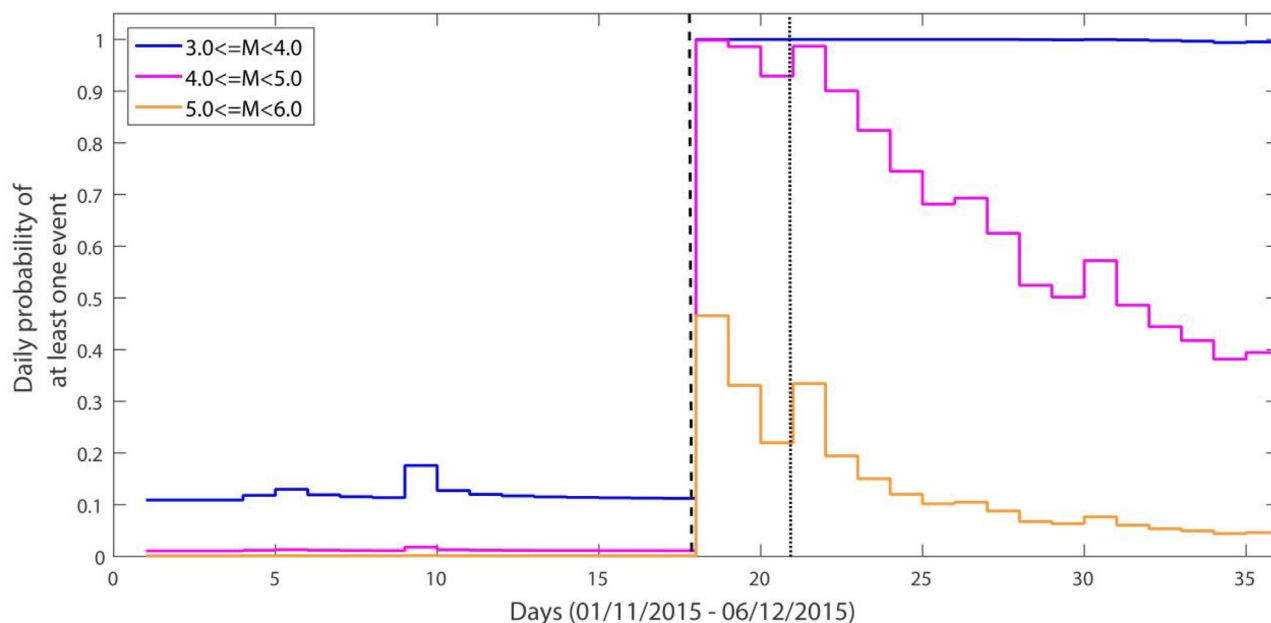

Figure 5. Daily probabilities of one or more events with $3.0 \leq M < 4.0$, $4.0 \leq M < 5.0$, $5.0 \leq M < 6.0$ with blue, violet and orange lines, respectively, for the time period from the 1st of November 2015 until the 6th of December 2015. The region for which these probabilities were calculated is the same as the region plotted in Fig. 2. The dashed line coincides with the first computation after the occurrence of the M_w 6.5 event of 17 November 2015. The dotted line coincides with the 21th of November where we can observe a jump in the plot.

not known, for initiating the rupture each cell is randomly assigned with a stress slip budget close to threshold. The stress is increased due to the tectonic loading and when it exceeds a certain value in a cell, then a rupture nucleates. After the nucleation, the slip budget in that cell is decreased by a constant value multiplied by the square root of the area of the expanding rupture. The rupture growth in the surrounding cells is evaluated by the changes in the Coulomb Failure Function (ΔCFF), either increases or decreases.

The rupture propagation and stopping are basically controlled by two free parameters: the strength reduction coefficient (S-R), which is a kind of weakening mechanism (Console *et al.* 2017, 2018) and the aspect ratio coefficient (A-R); which works as a limitation to the rupture expansion (Console *et al.* 2017, 2018). When increasing the S-R parameter the rupture is enhanced. It is equivalent to the role of the free parameter η in the Virtual Quake Simulator developed for California (Schultz *et al.* 2017), with value of $\eta = 0.5$ meaning that the nearby element requires
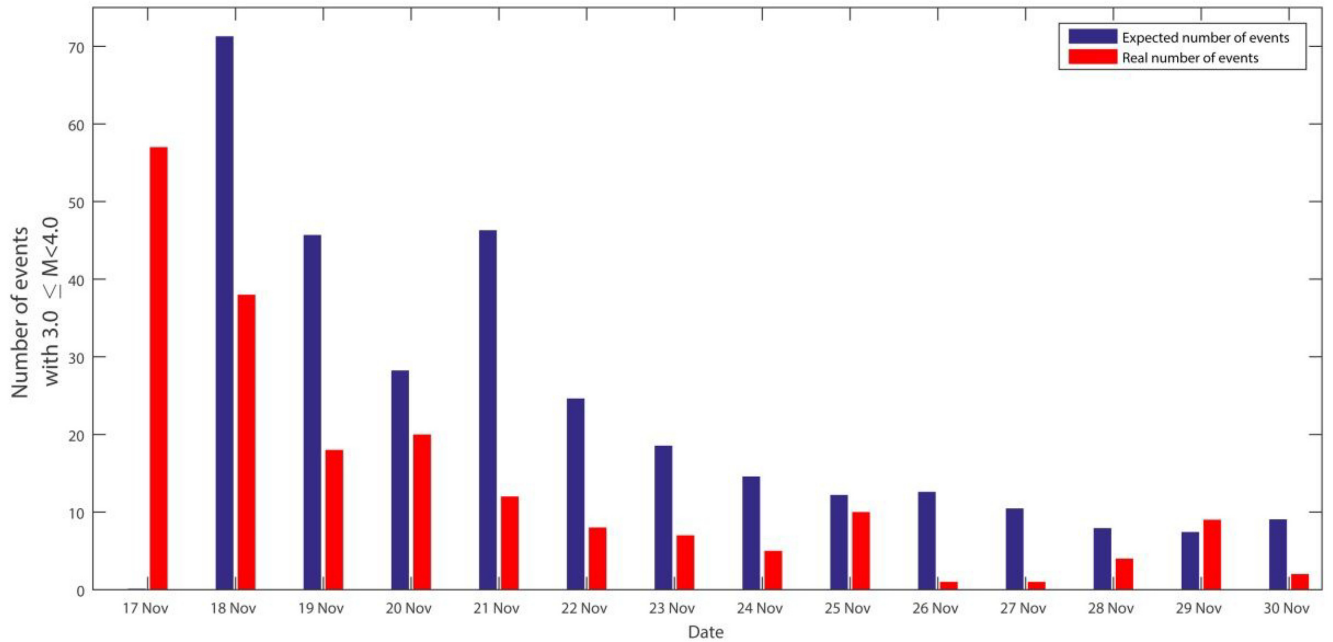
Figure 6. Expected and real number of events with $3.0 \leq M < 4.0$, per day, under the clustering model with the parameters obtained from the best fist, for 2 weeks after the occurrence of the M_w 6.5 event of the 17th November.
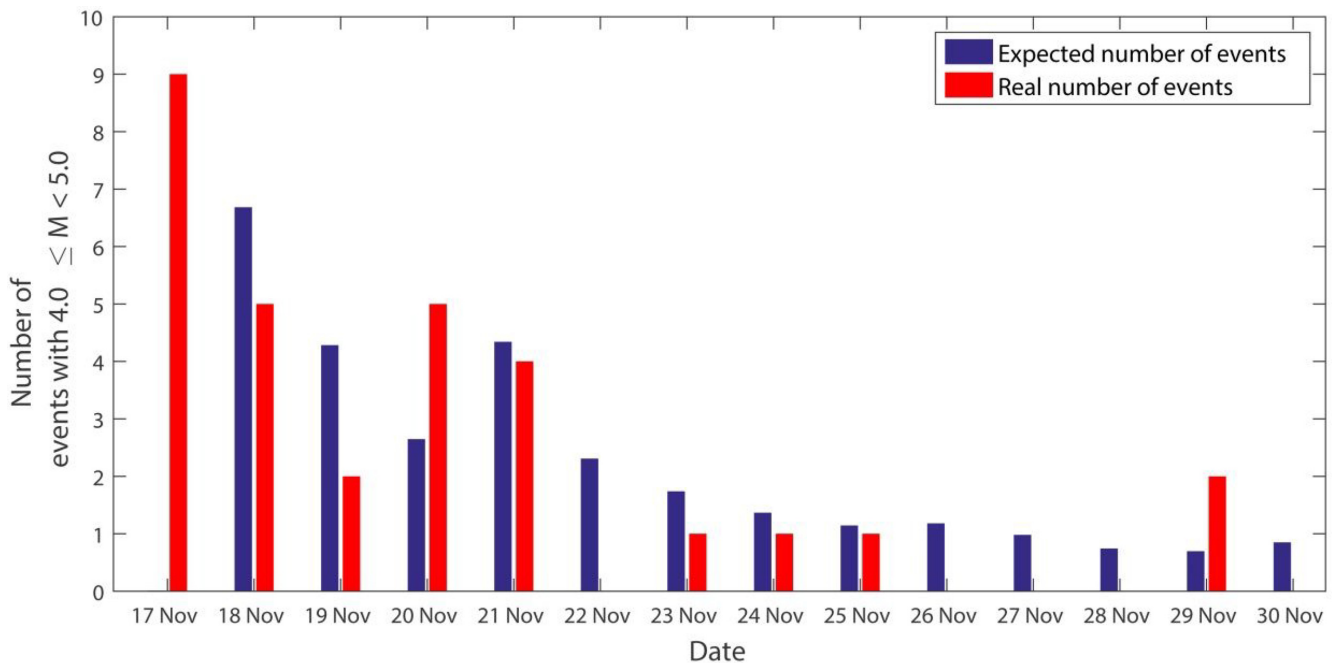

Figure 7. Expected and real number of events with $4.0 \leq M < 5.0$, per day, under the clustering model with the parameters obtained from the best fist, for 2 weeks after the occurrence of the M_w 6.5 event of the 17th November.

50 per cent of stress increase in order to join the rupture. This is also a value consistent with the UCERF2 fault model in Sachs *et al.* (2012) and in Tullis *et al.* (2012a, b). The parameter A-R, depending upon the width of the seismogenic layer, inhibits the propagation to exceed many times the width of the fault system. A rupture stops in the lack of any neighboring cell with stress exceeding the effective strength. During the rupture process, a cell can fail more than once. Rupture is also allowed to propagate through

neighboring fault segments according to the aforementioned rules within a maximum distance of some kilometers (for example 5, 10 km).

The simulation algorithm has been refined since its first version presented in Console *et al.* (2015). In the current version, the Rate and State Constitutive law (Dieterich 1994) is incorporated for a probabilistic assessment of the nucleation time of each earthquake. The seismicity rate in each cell is given as a function of the Coulomb
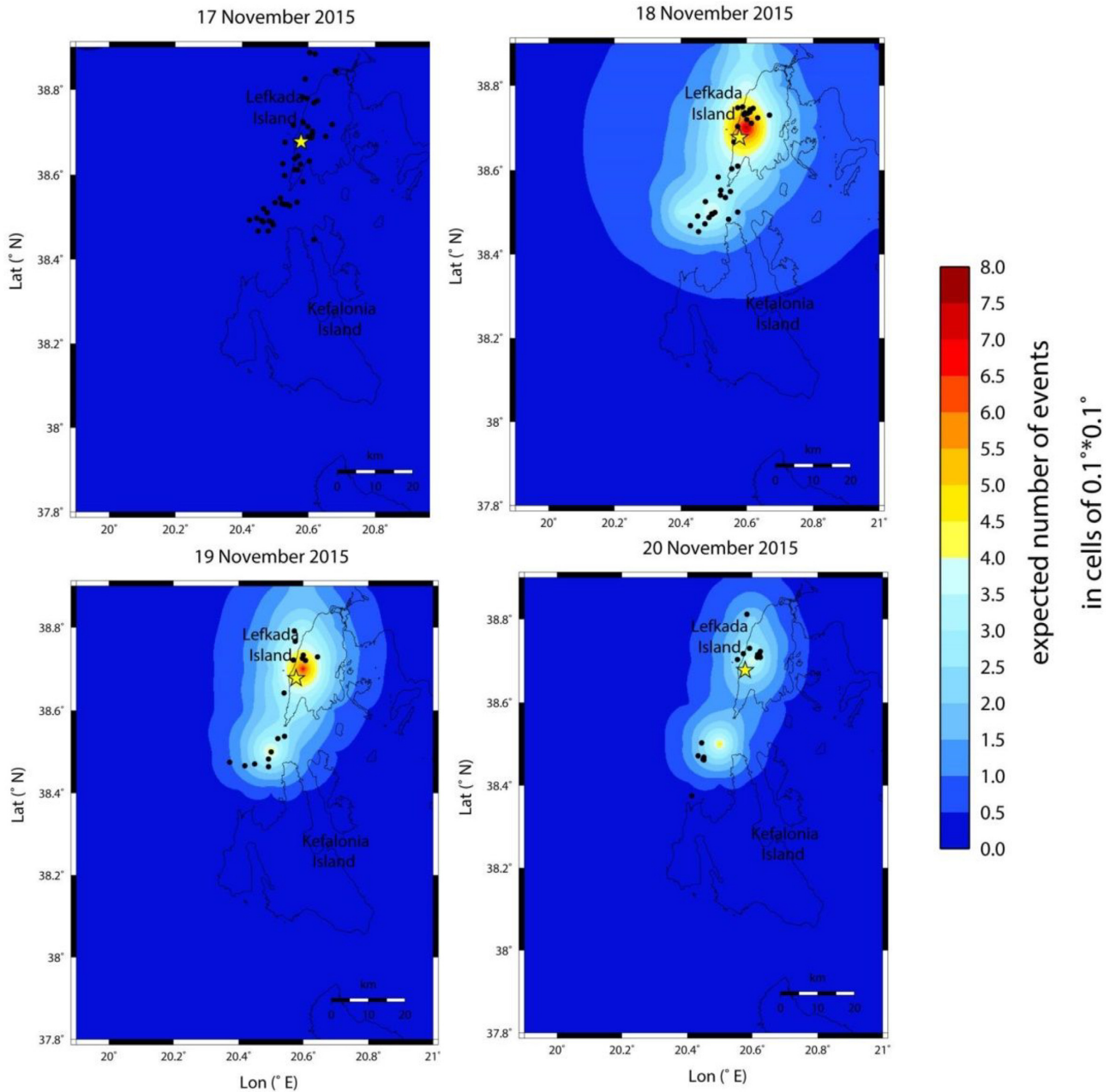
Figure 8. Expected number of events per day per cell of 0.1×0.1 degrees of events with $3.0 \leq M < 4.0$ at midnight before the occurrence of the main shock at 07:10:07 (GMT) and a few days afterward. The computations are performed at midnight of each day. The yellow star represents the epicentre of the main shock. The black dots represent the real number of events.

Failure Function change (ΔCFF) by the following relation:

$$R = \frac{r}{\left[\exp\left(-\frac{\Delta CFF}{A\sigma}\right) - 1\right] \exp\left(\frac{-\Delta t}{\gamma_0 A\sigma}\right) + 1}. \quad (1)$$

Coulomb stress changes are computed through the well-known relation (Rice 1993).

$$\Delta CFF = \Delta\tau + \mu' \cdot \Delta\sigma_n, \quad (2)$$

where $\Delta\tau$ is the shear stress change computed in the slip direction, $\Delta\sigma_n$ the normal stress change (positive for extension) and μ' the apparent friction coefficient.

In relation (1), r stands for the reference seismicity rate of the area under study and $\gamma_0 = \frac{1}{\dot{\tau}_r}$, where $\dot{\tau}_r$ is the reference shear stressing

rate and $A\sigma$ is the constitutive parameter. $A\sigma$ describes the instantaneous response of friction to a step change in slip change (Toda & Stein 2003) and is also inversely proportional to the characteristic decay time, t_a, according to the relation

$$t_a = \frac{A_\sigma}{\dot{\tau}_r}. \quad (3)$$

and the $A\sigma$ is introduced in the simulator code along with S-R and A-R.

A range of $A\sigma$ values between 0.0012 and 0.9 MPa is used in previous publications (see Table 2), inferred from seismicity patterns for different earthquake sequences (Harris 1998). The Rate and State Constitutive law is used at the step before the nucleation when we compute the minimum time needed to exceed the stress
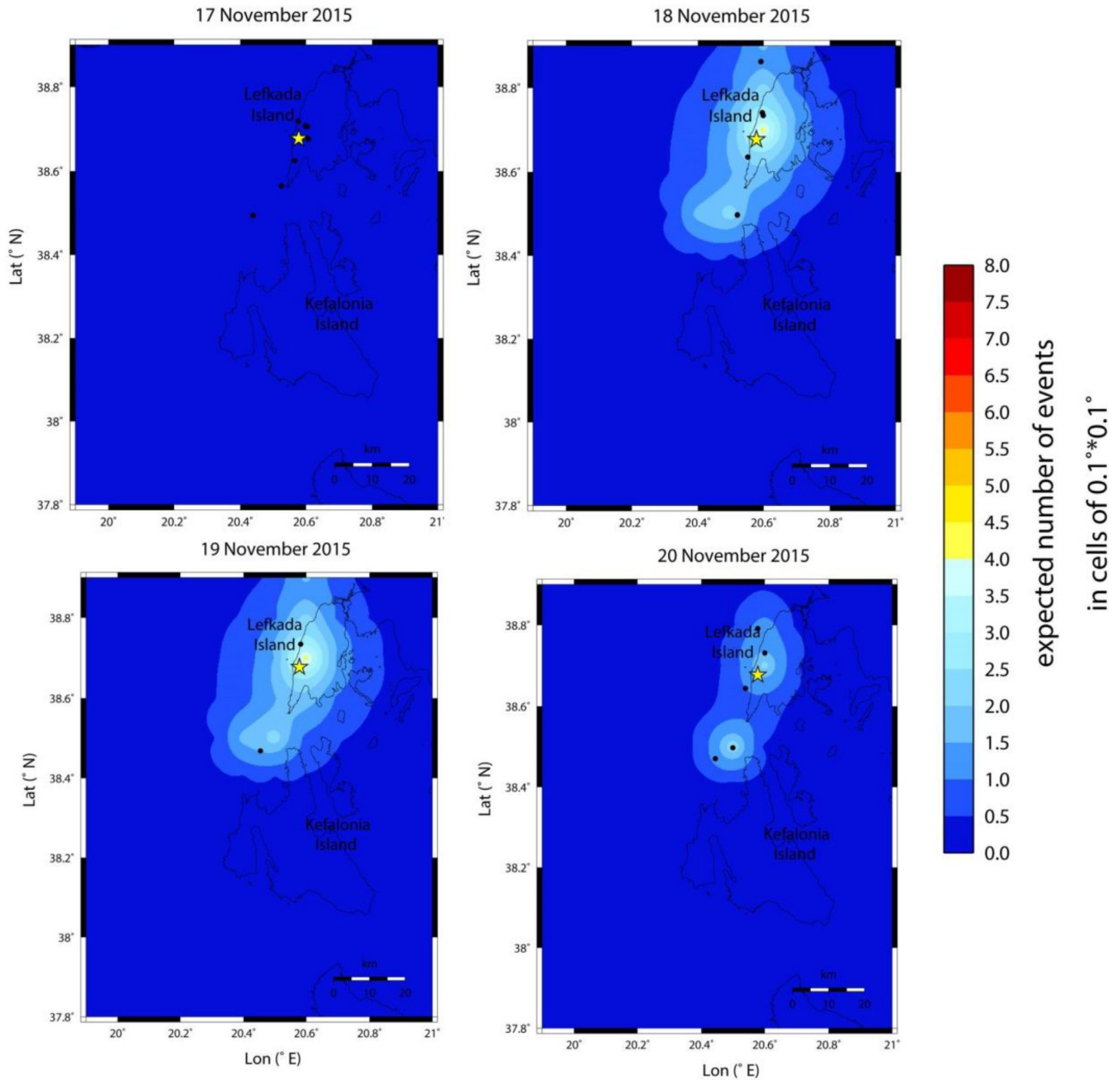
Figure 9. Expected number of events per day per cell of 0.1×0.1 degrees of events with $4.0 \leq M < 5.0$ at midnight before the occurrence of the main shock at 07:10:07 (GMT) and a few days afterward. The computations are performed at midnight of each day. The yellow star represents the epicentre of the main shock. The black dots represent the real number of events.

threshold on any cell. After setting an initial Δt, we compute the occurrence probability in each cell and when it exceeds a random number between 0 and 1, then the stress budget is increased according to the available slip rates, and a new rupture is nucleated.

5 APPLICATION OF THE ETAS MODEL TO THE CENTRAL IONIAN ISLANDS

Since the area of the Central Ionian Islands exhibits high seismic activity and strong ($M \geq 6.0$) main shocks are remarkably frequent, we may take the opportunity to test the performance of the ETAS model and prove its validity in a retrospective way. The data used are taken from the catalogue compiled by the Geophysics Department of the Aristotle University of Thessaloniki (GD–AUTh)

(http://geophysics.geo.auth.gr/ss/station_index_en.html) based on the recordings of the Hellenic Unified Seismological Network (HUSN). It is generally accepted that a test of a forecasting hypothesis should be carried out using a completely different data set than the one used during the formulation of the hypothesis. For this reason when applying the ETAS model we split the data set into learning and testing periods, and here in particular, two different learning and testing periods are chosen (Table 3).

Learning periods should include the largest and longest possible complete data set with at least one strong main shock. Both testing periods start just before the occurrence of the main shock to be tested. The first learning period is from January 2008 until October 2015 for the corresponding testing period to include the M_w6.5 17 November 2015 Lefkada main shock. The second learning period
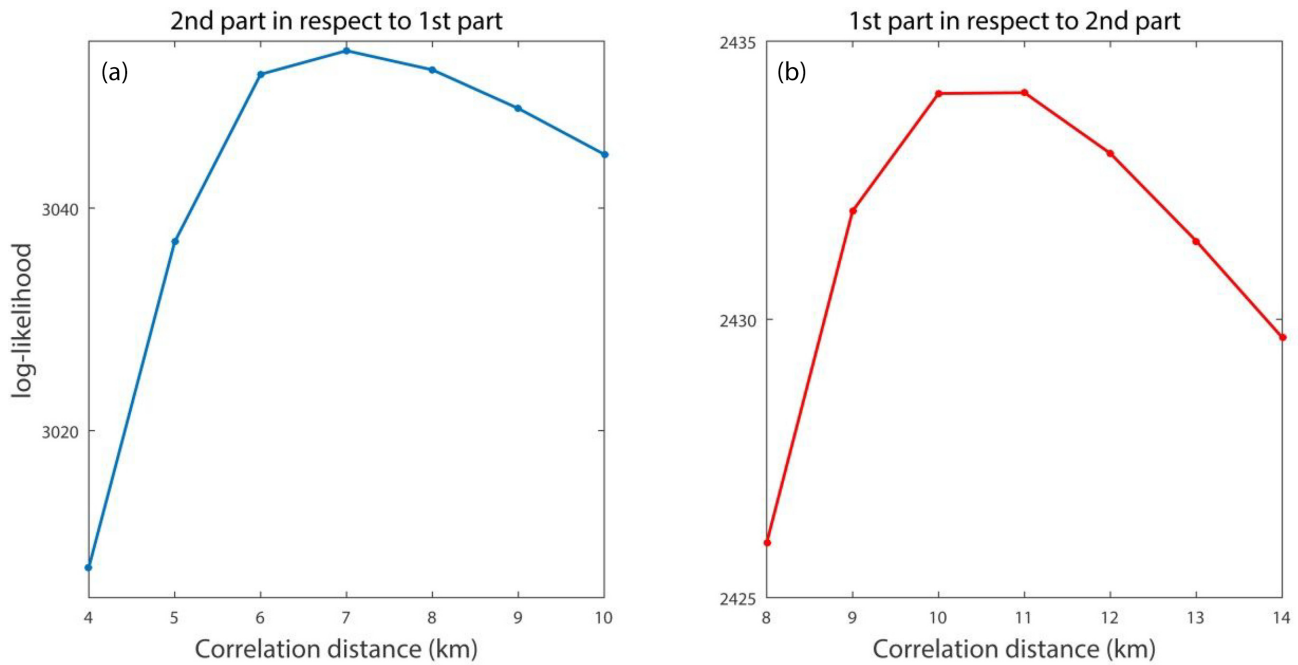
Figure 10. (a) Plot of the likelihood of the second part of the catalogue under the time-independent Poisson model created from the first part of the catalogue, versus different values of the c parameter of the smoothing algorithm. (b) Equivalent plot for the first part of the catalogue in respect to the second.
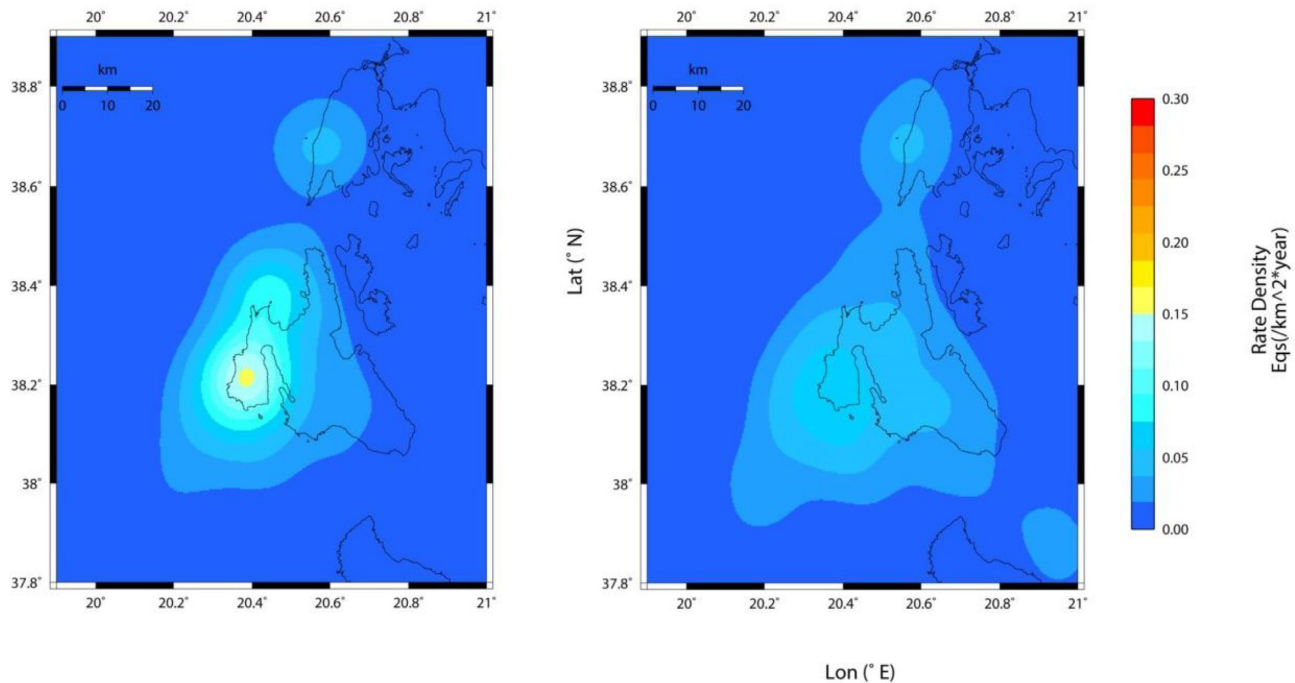

Figure 11. Smoothed distribution of the Central Ionian Islands (01 January 2008–29 January 2014) seismicity obtained by the smoothing algorithm applied to the (a) raw catalogue (b) weighted catalogue with the model parameters shown in the last column of Table 9. The colour scale represents the number of events occurred in cells 1 km x 1 km wide over the total duration of the catalogue.

includes only the first main shock of the 2014 Kefalonia doublet, which occurred on 26 January, with M_w 6.1, so as to test the performance of the ETAS model on the second main shock, which occurred on 03 February 2014, with M_w 6.0. The learning period thus includes the events that occurred from 01 January 2008 until 29 January 2014, just a few days before the second main shock.

5.1 Application in the first learning and testing period

The completeness of the catalogue for the learning period of January 2008–October 2015, is examined through the application of the goodness-of-fit method (Wiemer & Wyss 2000). The magnitude of completeness for the learning period is found equal to $M_c = 2.8$ and the catalogue includes 2022 events above this threshold. This

Table 5. Values obtained for the parameters of the epidemic model under the second learning period in the progressive adjustment of the background seismicity.

Parameters	Number of iterations						
	1st	2nd	3rd	4th	5th	6th	7th
k (d^{p-1}), Productivity coefficient	0.1164	0.1019	0.1014	0.0958	0.0934	0.0415	0.0335
d_0 (km), Characteristic distance in the spatial distribution	1.9097	1.9520	1.9539	1.9562	1.9658	2.1307	2.1307
q, Exponent of the spatial distribution	1.8658	1.8671	1.8920	1.8925	1.8923	1.9497	1.9496
c (d), Time constant in Omori law	0.01629	0.0106	0.0103	0.0105	0.0106	0.0125	0.0258
p, Exponent in Omori law	1.0382	1.0384	1.0398	1.0425	1.0435	1.1167	1.2028
α	0.4148	0.4155	0.4121	0.4145	0.4142	0.4046	0.3785
f_r Fraction of spontaneous events	0.2979	0.3287	0.3304	0.3323	0.3324	0.3761	0.4044
$\ln L$	12 641.06	12 677.92	12 678.51	12 679.01	12 679.32	12 689.13	**12 695.96**
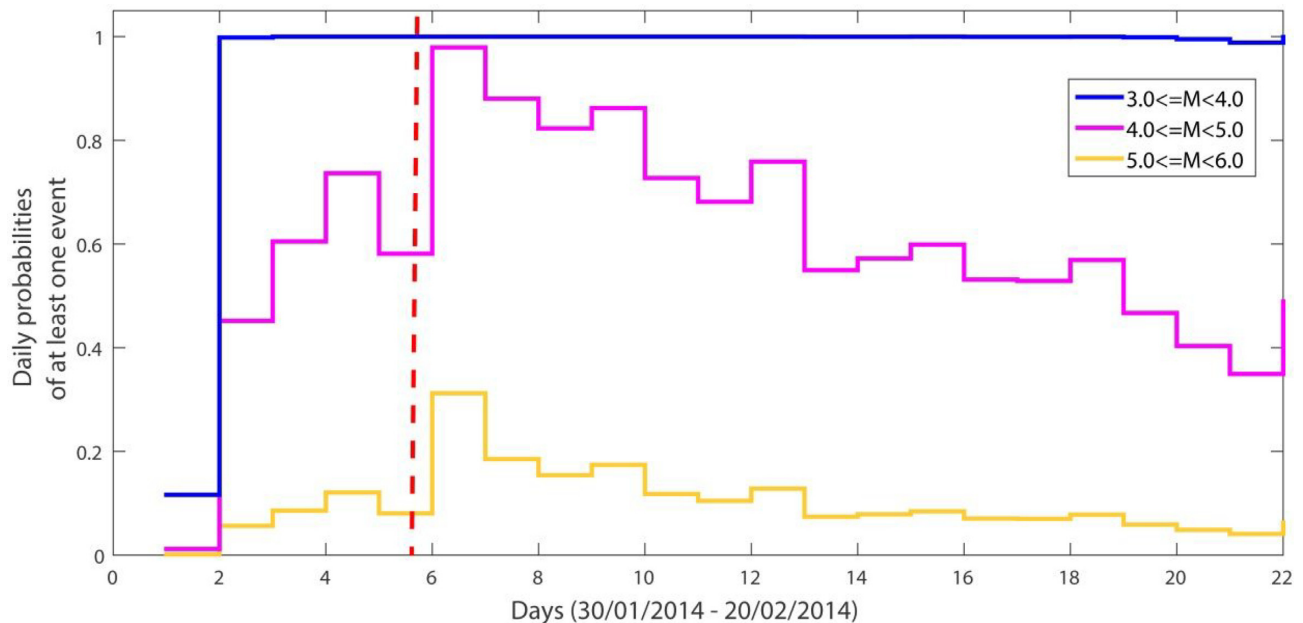
Figure 12. Daily probabilities of one or more events with $3.0 \leq M < 4.0$, $4.0 \leq M < 5.0$, $5.0 \leq M < 6.0$ with blue, violet and orange lines, respectively, for the time period from the 30 January 2014 until 22 February 2014. The region for which these probabilities were calculated is the same as the region plotted in Fig. 2. The red dashed line coincides with the first computation after the occurrence of the second event of the doublet on 3 February 2014.

is the minimum triggering magnitude considered. The b and a values, calculated via the maximum likelihood method proposed by Aki (1965), attain values of $b = 1.018 \pm 0.0005$ and $a = 6.155$. The standard deviation estimate is computed with the method introduced by Shi & Bolt (1982). The catalogue errors in geographical coordinates are ± 0.1, a value that is compatible with the spatial grid used in our study.

If we divide the catalogue from the 1st of January 2008 until the 31st of October 2015 into two parts with the same number of events, the second half including 1011 events covers just 20 per cent of the catalogue duration, due to the intense aftershock activity, which would lead us to biased estimations of the correlation distance. For this reason, a declustered catalogue (Reasenberg 1985) was used for finding the correlation distance d (Frankel 1995) In the study area no other model has been developed and applied that could be used as a reference model for the application of a more sophisticated method and stochastic declustering (e.g. Zhuang *et al.* 2002). Although defining the spatial and temporal extent of aftershock activity relative to the main shock may be based on rather subjective criteria in traditional declustering algorithms, like the one applied here, it is only used for estimating the correlation distance. For the rest of the computations the complete catalogue is

employed. The declustered catalogue of the period January 2008–October 2015 includes 710 events and the learning period is then divided into two parts, before and after 23 July 2010, each one including 355 events. As shown in Fig. 3, the process carried out using the smoothed seismicity obtained from the latest part of the catalogue over the former one, and vice versa (Console *et al.* 2010a), indicated the two optimal values equal to 6 and 11 km, respectively. Thus, the average value for the correlation distance adopted for the next calculations is $d = 8.5$ km.

The iterative process of Console *et al.* (2010a) is then used for estimating the parameters according to the maximum likelihood criterion. The best fit values obtained after four iterations are shown in Table 4. Using the parameters estimated after the final iteration, taking into account the highest value of the likelihood we may obtain the new smoothed distribution of the Central Ionian Islands seismicity (Fig. 4b). A comparison between the maps in Figs 4(a) and (b) obtained from the declustered catalogue clearly shows that the smoothed distribution applied to the weighted catalogue is more diffuse.

The testing period is chosen to start a few days before the 2015 M_w 6.5 Lefkada main shock for checking the performance of the epidemic model regarding the main shock and the subsequent events.
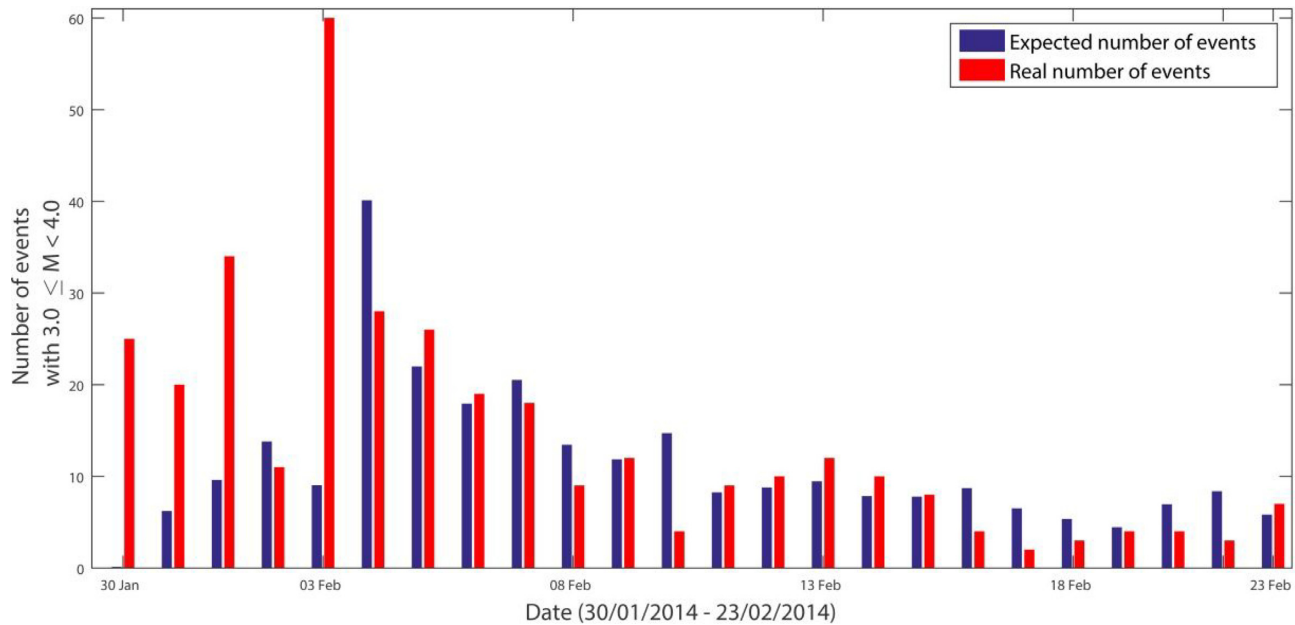
Figure 13. Expected and real number of events with $3.0 \leq M < 4.0$, per day, under the clustering model with the parameters obtained from the best fist, for 2 weeks after the occurrence of the M_w 6.5 event of the 17 November 2015.
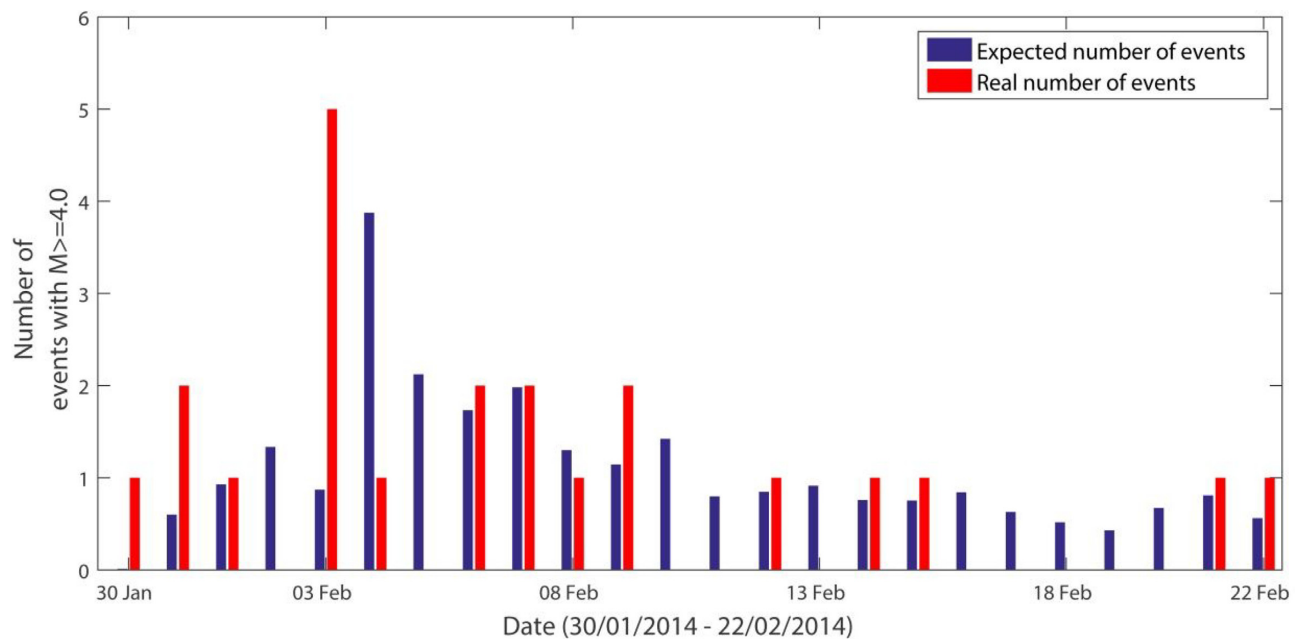

Figure 14. Expected and real number of events with $4.0 \leq M < 5.0$, per day, under the clustering model with the parameters obtained from the best fist, for 2 weeks after the occurrence of the M_w 6.5 event of the 17 November 2015.

Daily probabilities were calculated for a few days before and after the main shock. The absence of foreshocks is reflected in the plot (Fig. 5), and therefore, the occurrence probability for an event with $M \geq 6.5$ is relatively low at midnight, approximately 7 hr before the occurrence of the main shock, 2.91×10^{-5}. Fig. 5 shows the daily probabilities of one or more events within different magnitude ranges. The dashed line coincides with the first computations after the occurrence of the target event where the daily probabilities were significantly increased. The dotted line coincides with the 21st of

November where a jump in the plot is observed. This is probably due to the occurrence in the last day of five events with magnitudes $M \geq 4.0$.

A comparison between the observed and the expected earthquake frequency, is shown in Figs 6 and 7 for events with $3.0 \leq M < 4.0$ and $4.0 \leq M < 5.0$, respectively. We may see that the model soon before the occurrence of the target event returns low occurrence probabilities, meaning that there is no indication for an event occurrence. However, the model soon adjusts to the increased earthquake
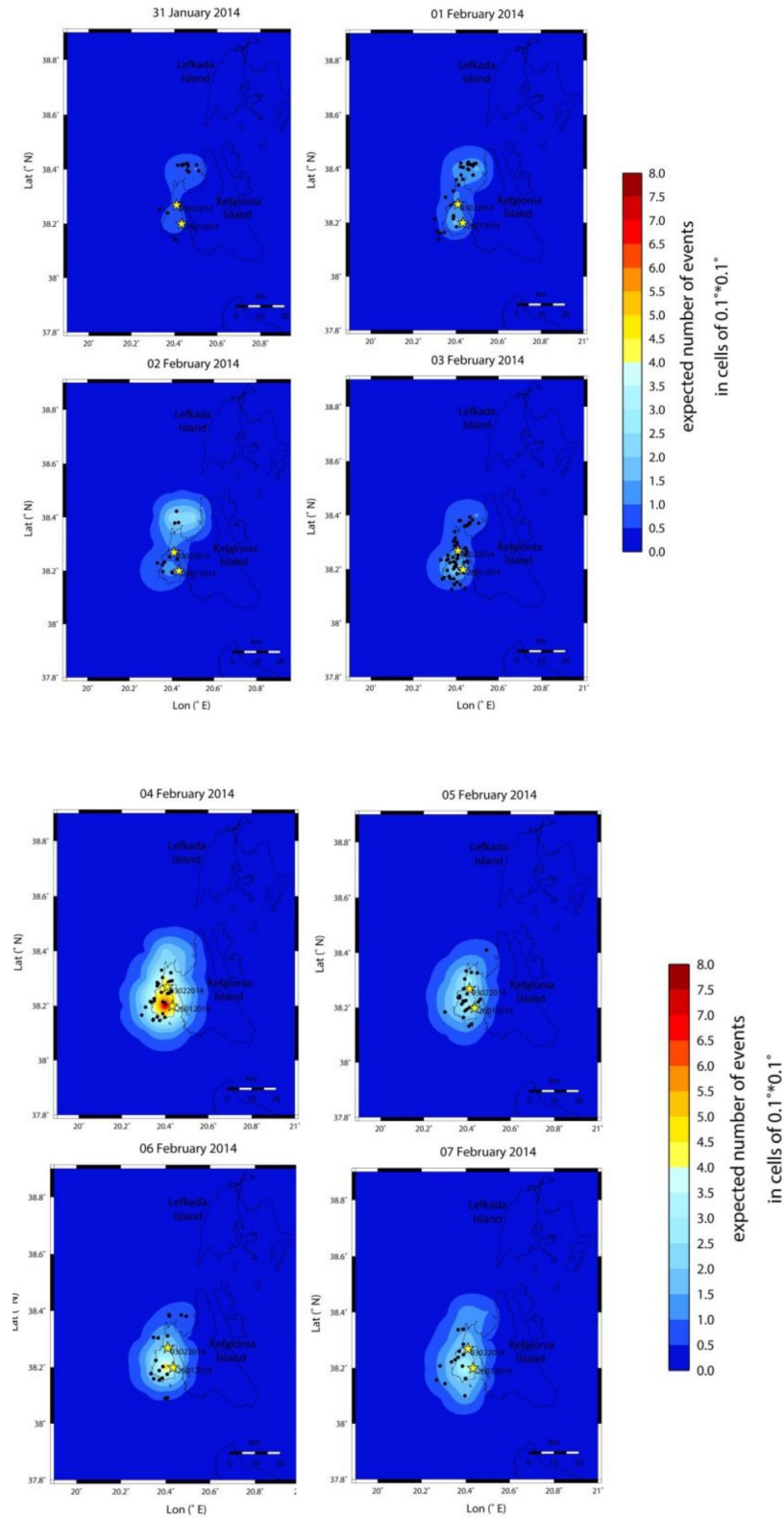
Figure 15. a, b. Expected number of events per day per cell of 0.1×0.1 degrees of events with $3.0 \leq M < 4.0$ from 31 January 2014 to 07 February 2014. The computations are performed at midnight of each day. The yellow star represents the epicentre of the main shocks of the doublet. The black dots represent the real number of events.

Table 6. Contingency table.

Forecasted	Observed	
	Yes	No
Yes	a	b
No	d	c

occurrence beginning with the main event. Although the number of expected events is in most cases larger than the observed one, the expected number tails off as the aftershocks do.

Time-dependent maps were constructed showing the expected number of events of $3.0 \leq M < 4.0$ and $4.0 \leq M < 5.0$ for several days after the main shock. As shown in the following maps (Figs 8 and 9), the spatial pattern of the expected earthquake number agrees well with the epicentral distribution of the occurring shocks.

5.2 Application in the second learning and testing period

One non-trivial case for testing the ETAS performance appears when intense seismic activity precedes the target event, as in the 2014 Kefalonia doublet. The first main shock of M_w 6.1 that occurred on the 26th of January 2014 is included in the learning period whereas the second main shock of the 3rd of February with M_w 6.0 is included in the testing period. We decided thus, to perform a second experiment and check again the model performance, since an objective test should be carried out on data with comparable magnitudes, that is a strong main shock should be contained in the learning phase. The learning data set for the fitting of the model parameters is the catalogue from the 1st of January 2008 up to the 29th January 2014. This data set can be considered complete above $M_c = 2.8$ and includes 1100 events with $M \geq 2.8$.

The same steps as in section 5.1 are followed for determining the correlation distance, catalogue declustering for the optimal values of the correlation distance to be as uniform as possible and the iterative adjustment of the background seismicity. The declustered catalogue includes 700 out of the 1100 events of the original catalogue and is divided into two parts each comprising 350 events of magnitude $M \geq 2.8$.

The plots of the correlation distance—likelihood indicate that the optimal value is $cd = 9$ km (Fig. 10), which is compatible with the value used in the previous computations (8.5 km). Using a grid size of 1 km we can create the model for the background seismicity (Fig. 11a), and with iterative process we performed seven iterations and found the best-fitting values (Table 5). Using the final estimated parameters we obtain the new smoothed distribution seismicity applied to the weighted catalogue (Fig. 11b). We may notice that the smoothed distribution obtained for the two learning phases are similar and more compatible, when compared to those obtained using the raw catalogue (see Figs 4b and 11b).

After the determination of the background seismicity, the second test is carried out. We ran the algorithm for the likelihood computation without looking for a best fit, just using the parameters obtained from the learning phase. As a result, at midnight, 3 hr before the occurrence of the second main shock of the doublet the probability of an event with $M \geq 6.0$ was 8.51E-03. Yet, after the occurrence of the target event of the 3rd February 2015, the daily probabilities change dramatically (Fig. 12). Figs 13 and 14 show the expected number of events according to the model compared to the observed number of events with $3.0 \leq M < 4.0$ and $4.0 \leq M < 5.0$, respectively. After the occurrence of the target event, the observed and

expected number of events are in good agreement, particularly for those with $3.0 \leq M < 4.0$. We may also observe in Fig. 14 that even though for five consecutive days no earthquakes in this magnitude range occurred, the increased seismicity rate affirms the relatively high values of the calculated probabilities. According to the time-dependent maps showing the expected daily seismicity rates, the spatial distribution of the expected events is in accordance with the observed ones (Figs 15a and b).

It is evident that for achieving better performance and a more successful forecast it is important to use catalogues containing earthquakes of lower magnitude than that of the main shock, for seismicity forecasting during an aftershock sequence. The catalogue for the learning period should also contain events in similar magnitude range to the events of the aftershock sequence. Otherwise, the model performance may systematically underestimate the aftershock occurrence rate. In order to avoid misleading computations, we should either use typical parameters provided from the application in an adjacent area or update the parameters adopted during the forecast process, if possible, before each computation.

6 VERIFICATION PROCEDURES

A model, in order to be considered valid, should be accompanied by robust and rigorous tests assessing its results (Console 2001). A common way of measuring the effectiveness of earthquake forecasts can be performed by means of a Pattern Informatics (PI) method that quantifies temporal variations in seismicity (Holliday *et al.* 2005, 2006a, b). This approach uses a classification scheme based on a binary criterion (forecast = yes or no, occurrence = yes or no) resulting in the construction of a 2 × 2 contingency table. The contingency table is built dividing the whole space-time volume of the test in numerous cells and reporting if in each cell a forecast was issued or not and an earthquake occurred or not.

In Table 6, *a* stands for the number of successful forecasts, *b* stands for the number of false alarms, *c* stands for the number of successful cases of non-occurrence and no forecasts and *d* stands for the missed alarms, that is the number of events that occurred but were not predicted. Then, based on the contingency table, a number of quantities can be calculated for measuring the success of the predictions. Holliday *et al.* (2005) proposed the application of the ROC-diagram. This is a plot of the Hit Rate (H) versus the False Alarm Rate (F) over a range of different thresholds. It is expressed by the following relationships $H = a/(a + d)$ and $F = b/(b + c)$. H describes the fraction of events that occurred in an alarm cell, based on a predefined threshold and F the fraction of false alarms, that is events predicted that have not actually occurred. A forecasting method is working well if $H > F$, while $H = F$ corresponds to random predictions. Another test derived from the contingency table is the R- score (Hanssen & Kuipers 1965), which is based on the quantity $R = \frac{a}{a+b} - \frac{d}{c+d}$ that describes the difference between the proportion of successful forecasts and the proportion of the failed to be predicted. The values of R range between –1 and 1, where –1 means all the predictions are wrong, 1 means all the predictions are correct, both the positive and the negative ones and 0 corresponds to the random predictions. Based on a similar idea, Shi *et al.* (2001) applied the R-score approach using a different relation with equivalent interpretation: $R' = \frac{a}{a+d} - \frac{b}{b+c}$.

Our study area is divided into 132 square cells of 0.1° × 0.1°, whereas the verification period is divided into bins of 24 hr each. In order to minimize as much as possible the computational burden, the verification periods that correspond to the two learning periods, in

Table 7. Contingency table for the ETAS model corresponding to the verification period 01 November 2015–31 January 2016 using various occurrence rate thresholds.

	r = 0.1		r = 0.01		r = 0.001	
Forecasted	Observed		Observed		Observed	
	Yes	No	Yes	No	Yes	No
Yes	a = 12	b = 22	a = 21	b = 460	a = 21	b = 2631
No	d = 20	c = 12 102	d = 11	c = 11 664	d = 11	c = 9493

Table 8. Contingency table for the ETAS model corresponding to the verification period 30 January 2014–30 March 2016 using various occurrence rate thresholds.

	r = 0.1		r = 0.01		r = 0.001	
Forecasted	Observed		Observed		Observed	
	Yes	No	Yes	No	Yes	No
Yes	a = 13	b = 56	a = 24	b = 733	a = 24	b = 4192
No	d = 12	c = 7845	d = 1	c = 7168	d = 1	c = 3709

Table 9. Results from the application of the tests for both verification periods and various occurrence rate thresholds.

1st Verification period			2nd Verification period		
r = 0.1	r = 0.01	r = 0.001	r = 0.1	r = 0.01	r = 0.001
H = 0.520	H = 0.960	H = 0.960	H = 0.375	H = 0.656	H = 0.656
F = 0.007	F = 0.093	F = 0.530	F = 0.002	F = 0.038	F = 0.217
R = 0.186	R = 0.032	R = 0.006	R = 0.351	R = 0.042	R = 0.007
R' = 0.513	R' = 0.867	R' = 0.430	R' = 0.373	R' = 0.618	R' = 0.439

Table 10. Information on the location, geometry, slip and dimensions of the fault segments of the Central Ionian Islands fault system.

Name	Latitude (°N)	Longitude (°E)	Strike (°)	Dip (°)	Rake (°)	Length (km)	Width (km)	Slip rate (mm yr^{-1})
Lefkada North	38.698	20.562	18	60	185	16	10	10
Lefkada South	38.555	20.490	22	64	179	17	10	10
Kefalonia North	38.264	20.369	12	57	157	11	10	25
Kefalonia South	38.150	20.335	12	57	157	13	10	25
Offshore Kefalonia	37.915	20.085	40	45	168	33	20	25
Stepover 1	38.415	20.415	85	65	28	7	7	8
Stepover 2	38.472	20.460	85	65	28	7	7	8
Stepover 3	38.527	20.493	85	65	28	7	7	8

accordance with them, are 01 November 2015–31 December 2015 and 30 January 2014–30 March 2014. The magnitude threshold is set $M_{th} = 4.0$ resulting in 32 and 26 target events, respectively. Finally, for the filling of the contingency tables, the occurrence rate threshold is set equal to $r = 0.1$, $r = 0.01$ and $r = 0.001$ for both cases. Table 7 shows the results for the first verification period. The fraction of successful predictions in the case where the threshold is set equal to $r = 0.1$ is sufficiently high ($H = 0.375$) and, in parallel, the fraction of false alarms is particularly low ($F = 0.002$). The R-scores, according to the two alternative formulations, are also adequately high ($R = 0.351$ and $R' = 0.373$) suggesting that the predictions are far from being random. The results are similar when we come to the second verification period (Table 8). The fraction of successful predictions in the case of $r = 0.1$ is calculated to be $H = 0.52$ while the fraction of false alarms is negligible, $F = 0.007$. Regarding the R-scores, the values $R = 0.186$ and $R' = 0.513$ suggest that the forecasting procedure works sufficiently well. The equivalent results are displayed in Table 9.

When the occurrence rate threshold becomes lower, the fraction of successful results gets higher, but in that way, the fraction of false alarms also gets bigger. The policy for the best strategy should

be based on a balance between the cost of false alarms and that of missed ones. The results of our tests indicate that quantitative and reliable information regarding short-term earthquake occurrence based on the ETAS model may be provided to decision makers in order to be used for practical purposes.

7 APPLICATION OF THE EARTHQUAKE SIMULATOR TO THE CENTRAL IONIAN ISLANDS SEISMICITY

The eight rectangular fault segments comprising the fault system of the study area are discretized into square cells of 0.5 km × 0.5 km and their characteristics are reported in Table 10. One key factor in the application is the minimum earthquake magnitude, the selection of which is based upon the assumption that each event provokes the rupture of at least two cells. The smallest magnitude generated by an earthquake rupturing two cells is approximately $M = 3.6$. The duration of all simulated catalogues was 10 kyr excluding a warm up period of 2 kyr.

The selection of the appropriate values for the parameters S-R, A-R and $A\sigma$, is also critical for the production of a simulated catalogue
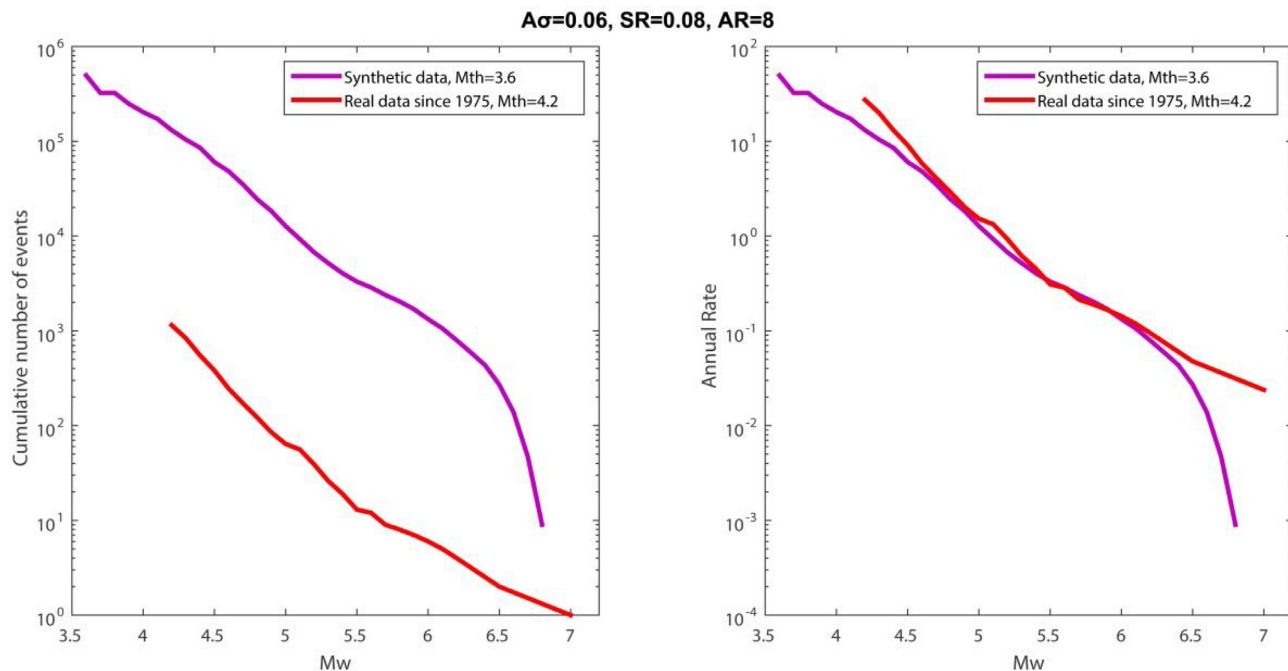
Figure 16. Left-hand panel: the frequency magnitude distribution and (right-hand panel) the annual rate of events using the synthetic data (magenta line) with $A\sigma = 0.06$ MPa, S-R $= 0.08$ and A-R $= 8$ and the real data since 1975 (red line).

Table 11. Input parameters of the simulations along with the *p*-value derived from the K–S test and the Wilcoxon rank-sum test.

Simulation	Maximum rupture aspect ratio	$A\sigma$ (MPa)	Strength reduction coefficient	*p*-value (K–S test)	*p*-value (Wilcoxon test)
1	8	0.09	0.12	0.9868	0.8126
2			0.10	0.9868	0.8286
3			0.08	0.9868	0.8609
4			0.06	0.9868	0.8609
5		0.08	0.12	0.9868	0.8286
6			0.10	0.9868	0.8447
7			0.08	0.9868	0.8771
8			0.06	1	0.8771
9		0.07	0.12	0.9868	0.8286
10			0.10	0.9868	0.8447
11			0.08	0.9868	0.8609
12			0.06	1	0.8771
13		0.06	0.12	0.9868	0.7966
14			0.10	0.9868	0.8447
15			0.08	1	0.8771
16			0.06	1	0.8609
17		0.05	0.12	0.9868	0.8286
18			0.10	0.9868	0.8286
19			0.08	1	0.8447
20			0.06	1	0.7966
21		0.04	0.12	0.8943	0.5848
22			0.10	0.8608	0.3588
23			0.08	0.6216	0.2358
24			0.06	0.6216	0.2199

representative of the observed seismicity. The reference earthquake catalogue was selected to be the one with $M_{th} = 4.2$ from 1975 to 2017. A significant thrust component contributes along with the strike slip motion to the final tectonic setting, explaining the upper limit of the ratio to a value equal to 8. The combination of $A\sigma = 0.06$ MPa, S-R $= 0.06$ and A-R $= 8$ is considered as the optimal 0one.

A simple comparison between the observed and the simulated data is attempted between the annual observed and calculated seismicity rate. Fig. 16(b) evidences the very good accordance between the two catalogues since the two lines almost coincide. Partial discrepancy between the simulated and the instrumental catalogue is observed in the high magnitude range (over 6.1). For a quantitative comparison, the methods used are the two-sample Kolmogorov–Smirnov (K–S) test (Kolmogorov 1933; Smirnov 1933) and the

Table 12. ETAS parameters estimated for different time periods of the simulated catalogue.

Time period (yr)	0–8	200–208	600–608	1000 -1008	1500–1508	2000–2008
f_r	0.7679	0.0370	0.7680	0.2307	0.0530	0.7700
K	0.0566	0.6770	0.0152	0.2240	0.1151	0.0147
d_0	1.2501	1.5280	2.1307	2.1300	2.1300	2.1307
q	2.3990	4.1698	1.9496	1.9400	1.9496	1.9496
c	10^{-6}	2.3900	10^{-6}	0.2350	1.3262	10^{-6}
p	4.0389	1.1170	1.2026	1.0308	1.1268	1.3400
α	0.0002	0.2957	0	0	0	0

Wilcoxon rank-sum test (Wilcoxon 1945), which is equivalent to a Mann–Whitney *U*-test (Mann & Whitney 1947). Both tests are presented in the Appendix B,with a significance level set to $\alpha = 0.05$. In our case, we compare the observed data since 1975 and the simulated data resulted from each attempt. Since the completeness magnitude for the observed data is $M_C = 4.2$, we compare the data in a range of magnitude from 4.2 to 6.5. Throughout our computations the *p*-values of the K–S test vary between 0.6216 and 1. In the case of the Mann–Whitney test, the *p*-values range from 0.2199 to 0.8771. The best values of the two tests are related to the same simulated catalogues (Table 11). As a final confirmation of our choice the *b*-values of the catalogues were tested, with the chosen catalogue getting a *b*-value equal to 1.16.

8 APPLICATION OF THE ETAS MODEL IN THE CENTRAL IONIAN ISLANDS SIMULATED SEISMICITY

The ETAS model is associated with short-term seismicity and for this reason we are mainly interested in small to moderate earthquakes. One way to fulfill this requirement and obtain smaller earthquakes generated by the simulator code is to loosen the constraints in its application. In order to decrease the magnitude threshold (M_{th}) of the simulated data as much as possible, we can allow the rupture of just one cell for the earthquake to be included in the analysis. The large duration of the synthetic catalogue may provide a large amount of data, but since we are interested in short-term interactions, it is more suitable to use simulated catalogues of much shorter duration, which is comparable to the real case. The learning periods set for examining the observational data approximately last 8 yr and this leads to the division of the simulated catalogue into smaller ones lasting 8 yr in order to compute the parameters of the ETAS model, compare them with the ones obtained from the observed data and test their sensitivity.

The first step includes the declustering method of Console *et al.* (2010a) for the iterative adjustment of the background seismicity. The most remarkable difference between the two cases is in the correlation distance. In reality, the correlation distance is computed about 9 km as it is shown in previous sections, but in the case of the simulations it is found about 1–2 km. This could be actually expected since it is probably due to the construction of the simulated catalogue. The simulator generates events inside pre-defined rectangles that do not cover the entire study area whereas the observed seismicity is more spatially spread. Thus, the correlation between events in the two parts of the simulated catalogue is obviously high since the spatial distribution in both cases exhibits remarkable similarity, with the epicentral concentration in the same areas.

Various periods of 8 yr were then used for the estimation of the ETAS parameters, as described in the Appendix A, in order to test if the estimated values are similar to the real case. The final

parameter values of the epidemic model, after achieving successful convergence, are presented in Table 12. The application of the ETAS model to the simulated catalogue reveals the sensitivity and the variability of the parameters when applied to different subcatalogues that are supposed to exhibit the same behaviour. The parameter α, which is related to the exponential magnitude law, is zero in most cases indicating that earthquakes produce the same number of offspring, regardless of their magnitude. The characteristic triggering distance, d_0, is estimated between 1.2 and 2.1 km, a value compatible to the observed case, as it is shown in previous sections, which does not seem to change much when the model is applied to different subcatalogues. The exponent of the spatial distribution q is approximately equal to 2, also without great variability. In contrast, the characteristics of the modified Omori law, and particularly the time constant, c, exhibit greater deviation showing that the spatial features are more stable than the temporal ones.

9 DISCUSSION AND CONCLUSIONS

The close spatiotemporal proximity of main shocks of $M_w \geq 6.0$ in the area of Central Ionian Islands motivated the investigation of retrospectively testing the validity of the ETAS model through the sequence of the 2015 M_w 6.5 Lefkada main shock and the 2014 Kefalonia doublet (M_w 6.1 and M_w 6.0). The model tests focused on the feasibility of reliable forecast of the main shocks, as well as whether the spatiotemporal behaviour of the aftershock sequences can be predicted.

Firstly, the 2015 M_w 6.5 Lefkada main shock and its aftershock sequence is tested, and then, the second main shock of the 2014 Kefalonia doublet is investigated after taking into account that the first one has occurred. The performance of the model regarding the aftershock sequences is remarkably good in both cases. Not only the number but also the locations of the observed events are consistent with the expected ones. Particularly in the second example, where a main shock is included in the last days of the learning period, the occurrence probabilities for earthquakes with $M \geq 4.0$ and $M \geq 5.0$ are high just before the occurrence of the target event. The probability of an event with $M \geq 6.0$ 3 hr before the occurrence of the second earthquake of the doublet is nearly 1 per cent, which is a relatively high value considering that it is several orders of magnitude larger than the background probability.

Complex observable spatial and temporal patterns of behaviour, like the earthquake occurrence, are difficult to understand and predict without knowledge of the underlying mechanisms and dynamics. A fundamental question is the accuracy of predictions and their validation in a quantitative way. We applied the *R*-score as the verification test for assessing our model performance. The results favour the use of the ETAS model for practical purposes, that is in order to track the evolution of aftershock sequences not only retrospectively but also in real time. In regions where the seismic hazard is high,

like in the case examined, daily forecasts could allow us to capture the variations in the seismicity and increased potential foreshock activity several hours before the occurrence of a strong event.

The combination of the ETAS model and the simulator code has provided some preliminary results showing that it is worth exploring more deeply the performance of the clustering model using the simulated catalogue generated through the physics-based simulator. Although the simulated data adequately match the observed ones as shown by statistical tests, some discrepancy is observed between the estimated parameters when the ETAS model is applied. This could be explained by the fact that the study period in the real case is characterized by intense seismic activity with three strong events ($M \geq 6.0$) in 8 yr, that is not the case in the subdivided periods of 8 yr in the simulated data. The aforementioned results shown in this paper encourage further investigation regarding physics-based simulators and their applicability that may reveal features and spatiotemporal patterns for short-term seismicity forecasting.

ACKNOWLEDGEMENTS

REFERENCES

Aki, K., 1965. Maximum likelihood estimate of b in the formula log n = a − bm and its confidence limits, *Bull. Earthq. Res. Inst.,* **43,** 99–103.

Belardinelli, M., Cocco, M., Coutant, O. & Cotton, F., 1999. Redistribution of dynamic stress during coseismic ruptures: Evidence for fault interaction and earthquake triggering, *J. geophys. Res.,* **104**(14), 925–945.

Catalli, F., Cocco, M., Console, R. & Chiaraluce, L., 2008. Modeling seismicity rate changes during the 1997 UmbriaMarche sequence (central Italy) through a rate- and statedependent model, *J. geophys. Res.,* **113,** B11301.

Console, R., 2001. Testing earthquake forecast hypotheses. *Tectonophysics,* **338,** 261–268.

Console, R., Carluccio, R., Papadimitriou, E. & Karakostas, V., 2015. Synthetic earthquake catalogs simulating seismic activity in the Corinth Gulf, Greece, fault system, *J. geophys. Res.,* **120**(1), 326–343.

Console, R., Chiappini, M., Minelli, L., Speranza, F., Carluccio, R. & Greco, M., 2018. Seismic hazard in Southern Calabria (Italy) based on the analysis of a synthetic earthquake catalog, *Acta Geophys.,* **66**(5), 931–943.

Console, R., Jackson, D.D. & Kagan, Y.Y., 2010a. Using the ETAS model for catalog declustering and seismic background assessment, *Pure appl. Geophys.,* **167,** 819–830.

Console, R. & Murru, M., 2001. A simple and testable model for earthquake clustering. *J. geophys. Res.,* **106,** 8699–8711.

Console, R., Murru, M. & Catalli, F., 2006a. Physical and stochastic models of earthquake clustering, *Tectonophysics,* **417,** 141–153.

Console, R., Murru, M. & Falcone, G., 2010b. Probability gains of an epidemic-type aftershock sequence model in retrospective forecasting of M ≥ 5 earthquake in Italy, *J. Seismol.,* **14**(1), 9–26.

Console, R., Murru, M. & Lombardi, A.M., 2003. Refining earthquake clustering models, *J. geophys. Res.,* **108,** 2468.

Console, R., Nardi, A., Carluccio, R., Murru, M., Falcone, G. & Parsons, T., 2017. A physics-based earthquake simulator and its application to seismic hazard assessment in Calabria (Southern Italy) region, *Acta Geophys.,* **65,** 243–257.

Console, R., Rhoades, D.A., Murru, M., Evison, F.F., Papadimitriou, E.E. & Karakostas, V., 2006b. Comparative performance of time-invariant, long range and short-range forecasting models on the earthquake catalogue of Greece, *J. geophys. Res.,* **111,** B09304.

Dieterich, J.H., 1994. A constitutive law for rate of earthquake production and its application to earthquake clustering, *J. geophys. Res.,* **99,** 2601–2618.

Dreger, D. & Savage, B., 1999. Aftershocks of the 1952 Kern County, California, earthquake sequence, *Bull. seism. Soc. Am.,* **89,** 1094–1108.

Evison, F.F. & Rhoades, D.A., 1993. The precursory earthquake swarm in New Zealand: Hypothesis tests, *New Zeal. J. Geol. Geop.,* **36,** 51–60.

Frankel, A., 1995. Mapping seismic hazard in the central and eastern United States, *Seismol. Res. Lett.,* **66**(4), 8–21.

Guatteri, M., Spudich, P. & Beroza, G., 2001. Inferring rate and state friction parameters from a rupture model of the 1995 Hyogo-ken Nanbu (Kobe) Japan earthquake, *J. geophys. Res.,* **106,** 26 511–26 521.

Hainzl, S. & Ogata, Y., 2005. Detecting fluid signals in seismicity data through statistical earthquake modeling, *J. geophys. Res.,* **110**.

Hanssen, A.W. & Kuipers, A.J.W., 1965. On the relationship between frequency of rain and various meteoroligical parameters, *Meded. Verh.,* **81,** 2–15.

Harris, R.A., 1998. Introduction to special section: stress triggers, stress shadows, and implications for seismic hazard, *J. geophys. Res.,* **103,** 24–24358.

Harris, R.A. & Simpson, R.W., 1998. Suppression of large earthquakes by stress shadows: a comparison of Coulomb and rate-and-state failure, *J. geophys. Res.,* **103,** 24–24451.

Helmstetter, A., Jackson, D.D. & Kagan, Y.Y., 2006. Comparison of short-term and time-independent earthquake forecast models for southern California, *Bull. seism. Soc. Am.,* **96**(1), 90–106.

Helmstetter, A., Kagan, Y.Y. & Jackson, D.D., 2005. Importance of small earthquakes for stress transfers and earthquake triggering, *J. geophys. Res.,* **110,** B05S08.

Helmstetter, A. & Sornette, D., 2003. Foreshocks explained by cascades of triggered seismicity, *J. geophys. Res.,* **108**(B10), 2457.

Helmstetter, A., Sornette, D. & Grasso, J. -R., 2003. Mainshocks are aftershocks of conditional foreshocks: How do foreshock statistical properties emerge from aftershock laws?, *J. geophys. Res.,* **108,** 2046.

Holliday, J.R., Nanjo, K.Z., Tiampo, K.F., Rundle, J.B. & Turcotte, D.L., 2005. Earthquake forecasting and its verification, nonlinear processes in geophysics, *European Geosciences Union (EGU),* **12**(6), 965–977.

Holliday, J.R., Rundle, J.B., Tiampo, K.F., Klein, W. & Donnelan, A., 2006a. Systematic procedural and sensitivity analysis of the pattern informatics method for forecasting large (M ≥ 5) earthquake events in southern California, *Pure appl. Geophys.,* **163**(11–12), 2433–2454.

Holliday, J.R., Rundle, J.B., Tiampo, K.F., Klein, W. & Donnelan, A., 2006b. Modification of the pattern informatics method for forecasting large earthquake events using complex eigenvectors, *Tectonophysics,* **413,** 87–91.

Jordan, T., 2006. Earthquake predictability, brick by brick, *Seismol. Res. Lett.,* **77**(1), 3–6.

Kagan, Y.Y. & Jackson, D.D., 1998. Spatial aftershock distribution: effect of normal stress, *J. geophys. Res.,* **103,** 24 453–24 467.

Karakostas, V., 2008. Relocation of aftershocks of the 2003 Lefkada sequence: Seismotectonic implications, in *Proceedings of the 3rd Hellenic Conf. Earthquake Engineering and Engineering Seismology*, 5–7 November 2008, Athens, Greece, CD ROM, 16pp.

Karakostas, V., Papadimitriou, E., Mesimeri, M., Gkarlaouni, C. & Paradisopoulou, P. 2015. The 2014 Kefalonia doublet (Mw6.1 and Mw6.0) central Ionian Islands, Greece: seismotectonic implications along the Kefalonia transform fault zone, *Acta Geophys.,* **63,** 1–16.

Karakostas, V.G. & Papadimitriou, E.E., 2010. Fault complexity associated with the 14 August 2003 Mw6.2 Lefkada, Greece, aftershock sequence, *Acta Geophys.,* **58,** 838–854.

Karakostas, V.G., Papadimitriou, E.E. & Papazachos, C.B., 2004. Properties of the 2003 Lefkada, Ionian Islands, Greece, earthquake seismic sequence and seismicity triggering, *Bull. seism. Soc. Am.,* **94,** 1976–1981.

Keilis-Borok, V.I. & Kossobokov, V.G., 1987. Periods of high probability of occurrence of the world's strongest earthquakes, in *Computational Seismology,* Vol. **19,** pp. 45–43, Allerton Press.

Keilis-Borok, V.I. & Kossobokov, V.G., 1990. Premonitory activation of seismic flow: algorithm M8, *Phys. Earth planet. Inter.,* **61,** 73–83.

Kolmogorov, A.N., 1933. Sulla determinazione empirica di una legge di distribuzione, *Giornale 943 dell' Istituto Italiano degli Attuari,* **4,** 83–91.

Kossobokov, V.G., Keilis-Borok, V.I. & Smith, S.W., 1990. Localization of intermediate-term earthquake prediction, *J. geophys. Res.,* **95,** 19 763–19 772.

Kossobokov, V.G., Romashkova, L.L., Keilis-Borok, V.I. & Healy, J.H., 1999. Testing earthquake prediction algorithms: statistically significant advance prediction of the largest earthquakes in the Circum-Pacific, 1992–1997, *Phys. Earth planet. Inter.,* **111,** 187–196.

Leptokaropoulos, K.M., Papadimitriou, E.E., Orlecka-Sikora, B. & Karakostas, V.G., 2012. Seismicity rate changes in association with the evolution of the stress field in northern Aegean Sea, Greece, *Geophys. J. Int.,* **188,** 1322–1338.

Leptokaropoulos, K.M., Papadimitriou, E.E., Orlecka-Sikora, B. & Karakostas, V.G., 2016. An evaluation of Coulomb stress changes from earthquake productivity variations in the Western Gulf of Corinth, Greece. *Pure appl. Geophys.,* **173,** 49–72

Lombardi, A.M., Cocco, M. & Marzocchi, W., 2010. On the increase of background seismicity rate during the 1997 -1998 Umbria-Marche, central Italy, sequence: apparent variation or fluid-driven triggering?, *Bull. Seismol. Soc. Am.,* **100,** 1138–1152.

Maccaferri, F., Rivalta, E., Passarelli, L. & Jonsson, S., 2013. The stress shadow induced by the 1975–1984 Krafla rifting episode, *J. geophys. Res.,* **118,** 1109–1121.

Mann, H.B. & Whitney, D.R., 1947. On a test of whether one of two random variables is stochastically larger than the other, *Ann. Math. Stat.,* **18,** 50–60.

Marzocchi, W. & Lombardi, A.M., 2009. Real-time forecasting following a damaging earthquake, *Geophys. Res. Lett.,* **36,** L21302.

Murru, M., Console, R. & Falcone, G., 2009. Real time earthquake forecasting in Italy, *Tectonophysics,* **470,** 214–223.

Murru, M., Zhuang, J., Console, R. & Falcone, G., 2014. Short-term earthquake forecasting experiment before and during the L'Aquila (central Italy) seismic sequence of April 2009, *Ann. Geophys.,* **57**(6), S0649, doi:10.4401/ag-6583, 2014.

Nanjo, K.Z. *et al.*, 2012. Predictability study on the aftershock sequence following the 2011 tohoku-oki, japan, earthquake: first results, *Geophys. J. Int.,* **191**(2), 653–658.

Ogata, Y., 1983. Estimation of the parameters in the modified Omori formula for aftershock sequences by the maximum likelihood procedure, *J. Phys. Earth,* **31,** 115–124.

Ogata, Y., 1988. Statistical models for earthquake occurrences and residual analysis for point processes, *J. Am. Stat. Assoc.,* **83,** 9–27.

Ogata, Y., 1998. Space-time point-process models for earthquake occurrences, *Ann. Inst. Stat. Math.,* **50,** 379–402.

Ogata, Y., Katsura, K., Falcone, G., Nanjo, K.Z. & Zhuang, J., 2013. Comprehensive and topical evaluations of earthquake forecasts in terms of number, time, space, and magnitude, *Bull. seism. Soc. Am.,* **103**(3), 1692–1708.

Ogata, Y. & Zhuang, J., 2006. Space-time ETAS models and an improved extension, *Tectonophysics,* **413**(1-2), 13–23.

Papadimitriou, E., Karakostas, V., Mesimeri, M., Chouliaras, G. & Kourouklas, C., 2017. The Mw6.5 17 November 2015 Lefkada (Greece) earthquake: structural interpretation by means of the aftershock analysis, *Pure appl. Geophys.,* **174,** 3869–3888.

Papadimitriou, E.E., 2002. Mode of strong earthquake occurrence in central Ionian Islands (Greece). Possible triggering due to Coulomb stress changes generated by the occurrence of previous strong shocks, *Bull. seism. Soc. Am.,* **92,** 3293–3308.

Papazachos, B.C., Kiratzi, A.A. & Karakostas, B.G., 1997. Towards a homogeneous moment magnitude determination for earthquakes in Greece and the surrounding area, *Bull. seism. Soc. Am.,* **87,** 474–483.

Reasenberg, P.A., 1985. Second-order moment of central California seismicity, *J. geophys. Res.,* **90,** 5479–5495.

Rice, J.R., 1993. Spatio – temporal complexity of slip on a fault, *J. geophys. Res.,* **98,** 9885–9907.

Rundle, J.B. 1988. A physical model for earthquakes 1. Fluctuations and interactions, *J. geophys. Res.,* **93,** 6237–6254.

Rundle, J.B. *et al.*, 2005. A simulation-based approach to forecasting the next great San Francisco earthquake, *Proc. Natl. Acad. Sci. U.S.A.,* **102**(42), 15363–15367.

Sachs, M.K., Yikilmaz, M.B., Heien, E.M., Rundle, J.B., Turcotte, D.L. & Kellogg, L.H., 2012. Virtual California earthquake simulator, *Seismol. Res. Lett.,* **83**(6), 973–978.

Schorlemmer, D. *et al.*, 2018. The collaboratory for the study of earthquake predictability: achievements and priorities, *Seismol. Res. Lett.,* **89**(4), 1305–1313.

Schultz, K.W., Yoder, M.R., Wilson, J.M., Heien, E.M., Sachs, M.K., Rundle, J.B. & Turcotte, D.L., 2017. Parametrizing phyisics-based earthquake simulations, *Pure appl. Geophys.,* **174,** 2269–2278.

Scordilis, E.M., Karakaisis, G.F., Karakostas, B.G., Panagiotopoulos, D.G., Comninakis, P.E. & Papazachos, B.C., 1985. Evidence for transform faulting in the Ionian Sea: the Cephalonia Island earthquake sequence, *Pure appl. Geophys.,* **123,** 388–397.

Shi, Y. & Bolt, B.A., 1982. The standard error of the magnitude-frequency b-value, *Bull. seism. Soc. Am.,* **72,** 1677–1687.

Shi, Y., Liu, J. & Zhang, G., 2001. An evaluation of Chinese annual earthquake predictions, 1990 -1998, *J. Appl. Probab.,* **38A,** 222–231.

Smirnov, N.V., 1933. Estimate of deviation between empirical distribution functions in two independent samples, *Bull. Moscow Univ.,* **2,** 3–16.

Stein, R.S., 1999. The role of stress transfer in earthquake occurrence, *Nature,* **402,** 605–609.

Taroni, M., Marzocchi, W., Schorlemmer, D., Werner, M., Zechar, J.D., Wiemer, S., Heiniger, L. & Euchner, F., 2018. Prospective CSEP evaluation of 1-day, 3-month, and 5-year earthquake forecasts for Italy, *Seismol. Res. Lett.* **89**(4), 1251–1261.

Toda, S. & Stein, R.S., 2003. Toggling of seismicity by the 1997 Kagoshima earthquake couplet: a demonstration of time-dependent stress transfer, *J. geophys. Res.,* **108**(B12), 2567.

Toda, S., Stein, R.S., Reasenberg, P.A. & Dieterich, J.H., 1998. Stress transferred by the Mw = 6.5 Kobe, Japan, shock: effect on aftershocks and future earthquake probabilities, *J. geophys. Res.,* **103,** 24–24 565.

Tullis, T.E., 2012. Preface to the focused issue on earthquake simulators, *Seismol. Res. Lett.,* **83**(6), 957–958.

Tullis, T.E. *et al.*, 2012a. Generic earthquake simulator, *Seismol. Res. Lett.,* **83**(6), 959–963.

Tullis, T.E. *et al.*, 2012b. Comparison among observations and earthquake simulator results for the allcal2 California fault model, *Seismol. Res. Lett.,* **83,** 994–1006.

Utsu, T., Ogata, Y. & Matsu'ura, R.S., 1995. The centenary of the Omori formula for a decay law of aftershock activity, *J. Phys. Earth,* **43,** 1–33.

Vere-Jones, D., Ben-Zion, Y. & Zuniga, R., 2005. Statistical seismology, *Pure appl. Geophys.,* **162,** 1023–1026.

Wessel, P., Smith, W.H.F., Scharroo, R., Luis, J. & Wobbe, F., 2013. Generic mapping tools: improved version released, *EOS, Trans. Am. Geophys. Un.,* **94,** 409–410.

Wiemer, S. & Wyss, M., 2000. Minimum magnitude of completeness in earthquake catalogs: examples from Alaska, the western US and Japan, *Bull. seism. Soc. Am.,* **90,** 859–869.

Wilcoxon, F., 1945. Individual comparisons by ranking methods, *Biometrics,* **1,** 80–83

Wilson, J.M., Yoder, M.R., Rundle, J.B., Turcotte, D.L. & Schultz, K.W., 2017. Spatial evaluation and verification of earthquake simulators, *Pure appl. Geophys.,* **174,** 2279–2293.

Zhuang, J., Chang, C. -P., Ogata, Y. & Chen, Y.-I, 2005. A study on the background and clustering seismicity in the Taiwan region by using a point process model, *J. geophys. Res.,* **110,** B05S13.

Zhuang, J., Christophersen, A., Savage, M.K. & Vere-Jones, D.D., 2008. Differences between spontaneous and triggered earthquakes. Their influences on foreshock probabilities, *J. geophys. Res.,* **113,** B11302.

Zhuang, J., Murru, M., Falcone, G. & Guo, Y., 2018. An extensive study of clustering features of seismicity in Italy from 2005 to 2016, *Geophys. J. Int.,* **216**(1), 302–318.

Zhuang, J., Ogata, Y. & Vere-Jones, D., 2002. Stochastic declustering of space-time earthquake occurrence, *J. Am. Stat. Assoc.,* **97**(3), 369–380.

Zhuang, J., Ogata, Y. & Vere-Jones, D., 2004. Analyzing earthquake clustering features by using stochastic reconstruction, *J. geophys. Res.,* **109**(3), B05301.

APPENDIX A: THE CLUSTERING MODEL

The epidemic model is based on the assumption that every earthquake is potentially triggered by all the previous ones and can trigger subsequent events according to their relative time–space distance. Seismicity is represented as the superposition of spontaneous and triggered events. The expected rate density of earthquakes, λ, is written as

$$\lambda\,(x, y, t, m) = f_r\,\lambda_0\,(x, y, m)$$
$$+ \sum_{i=1}^{N} H\,(t - t_i)\,\lambda_i\,(x, y, t, m)\,, \qquad (A1)$$

where f_r is the failure rate, that is the fraction of spontaneous events, $\lambda_0(x, y, m)$ is the time-invariant background seismicity, t_i is the occurrence time of the i event in a set of N earthquakes, $H(t)$ is the step function, such as $H\,(t) = 0$ for $t \leq 0$ and $H\,(t) = 1$ for $t > 0$ and $\lambda_i(x, y, t, m)$ is the kernel of the previous earthquakes. The first term of the right hand side represents the 'independent' seismicity and the second part the 'triggered' seismicity, in probabilistic terms. It means that each earthquake is not completely either dependent or independent, but connected to all previous events and to the background seismicity, according to different weights.

The spontaneous, 'background', seismicity follows the Gutenberg–Richter law

$$\lambda_0\,(x, y, m) = \mu_0\,(x, y)\,\beta e^{-\beta(m - m_0)}, \qquad (A2)$$

where $\mu_0(x, y)$ is the spatial density of earthquakes of magnitude $m \geq m_0$, m_0 is the completeness magnitude and β is connected to the b-value of the G–R law as $\beta = b\,ln(10)$.

The occurrence rate density of subsequent events in time dependent seismicity encompasses time, magnitude and space components

$$\lambda_i\,(x, y, t, m) = K h\,(t - t_i)\,\beta e^{-\beta(m - m_i)}\,f\,(x - x_i, y - y_i)\,, \quad (A3)$$

where K is a constant, $h(t)$ is the time and $f(x, y)$ the space distribution.

The time distribution is given by the modified Omori law (Ogata 1983):

$$h\,(t) = (p - 1)\,c^{p-1}(t - c)^{-p}, \quad p > 1 \qquad (A4)$$

describing the length of the time interval between a child and its parent. The exponent p defines the decay rate of aftershocks. When p increases, the decay gets faster. The parameter c is usually related to catalogue incompleteness at the beginning of the aftershock sequence, since immediately after a large earthquake the seismic network is saturated and many aftershocks are not recorded.

We model the spatial distribution of the triggered seismicity by a function $f(x_i, y_i)$ having circular symmetry around (x_i, y_i), which is the location of a triggering event of magnitude m_i and is normalized to 1. In polar coordinates, the spatial distribution is given by the equation

$$f\,(r, \theta) = \frac{(q - 1)}{\pi}\,\frac{d'^{2(q-1)}}{\left(r^2 + d'^2\right)^q}, \qquad (A5)$$

where r is the distance of (x, y) from (x_i, y_i), $d' = d_0\,e^{\alpha(m_i - m_0)}$, d_0 is the characteristic triggering distance for an earthquake of magnitude m_i and a is a free parameter. In that way, d and q are the two free parameters of the spatial distribution to be estimated. Many formulations of the spatial distribution can be found in the studies carried out during the last 20 yr (e.g. Console *et al.* 2003; Helmstetter *et al.* 2003; Zhuang *et al.* 2005; Ogata & Zhuang 2006).

Thus, the parameters to be estimated are: K (productivity coefficient), d_0 (characteristic triggering distance), q (exponent of the spatial distribution of induced events), α (coefficient of the exponential magnitude law), c (time constant of the generalized Omori law) and p (exponent of the generalized Omori law). The fraction of spontaneous events, f_r, is not a free parameter, but depends on the other ones and is constrained by the condition that the two parts of the eq. (A1) are equal, that is the total number of events expected for a particular set of parameters must be equal to the total number of events observed. The b-value is assumed to be constant over the geographical area spanned by the catalogue and is estimated independently from the other parameters.

For the background spatial distribution, we use an iterative adjustment proposed by Console *et al.* (2010a). This is the same kind of method suggested by Zhuang *et al.* (2002) differing only in the fact that in the latter, variable kernel functions are used to estimate the background rate. In the former, adopted here, in order to estimate the background rate, the Frankel's (1995) smoothing algorithm is used:

$$\check{N}_k = \frac{\sum_l N_l \exp\left(-\Delta_{kl}^2 \big/ d^2\right)}{\sum_l \exp\left(-\Delta_{kl}^2 \big/ d^2\right)}, \qquad (A6)$$

where N_l is the number of events in each cell centred on the l_{th} node, Δ_{kl} is the distance between nodes k and l, and d is a free parameter, named correlation distance. Using the above relation, a gridded smooth geographical distribution of the seismic rate density at each node k of a regular grid is created. Then, in order to obtain a continuous function, the single value of $\mu_0\,(x, y)$ is computed by interpolation between the four cells whose centres surround the point (x, y). The catalogue is divided in two parts and the parameter d is determined by maximizing the likelihood of the seismicity contained in the later half of the catalogue under the model obtained from the earlier half. The characteristic of this method is that the distinction between a spontaneous and a triggered event is made statistically. Instead of removing events from the catalogue, each event is assigned with a probability of being independent according to an algorithm based on the ETAS model.

As a first step, the maximum likelihood set of free parameters is found using the initial distribution of the smoothed seismicity $\lambda_0(x, y, m)$. Then the probability of independence p_i is computed, as the ratio between the independent component $f_r\lambda_0(x_i, y_i, m_i)$ and the composite rate density $\lambda(x_i, y_i, m_i, t_i)$ for every event i. A new distribution $\lambda_0(x, y, m)$ is computed using the weights p_i as a multiplying factor for each event, and dividing by f_r so that the distribution is normalized to the total number of events in the catalogue. The new smoothed distribution is used for a new best fit of parameters and so on until convergence is achieved.

APPENDIX B: THE STATISTICAL TESTS

The two-sample K–S test is a nonparametric test that evaluates the difference between the distributions $F(x)$ and $G(x)$ of the two data sample vectors over the range of x. The null hypothesis shows that the two data sets are from the same distribution and the alternative hypothesis that they come from different ones.

The test statistic is

$$D = \max_x \left(F(x) - G(x) \right). \tag{B1}$$

The decision to reject the null hypothesis is based on the asymptotic $p-$value by comparing it with the significance level α. If the $p-$value is greater than α then the null hypothesis cannot be rejected.

The Wilcoxon rank sum test is a non-parametric test, equivalent to the Mann–Whitney U-test, which compares two independent random variables F and G with sample sizes n and m, respectively, with the null hypothesis that $F = G$. The null hypothesis of the test is that the two samples were selected from populations having the same distribution. For the application of the test we rank the two samples. The Wilcoxon rank sum statistic T is

$$T_F = \sum_{i-1}^{n} R_{F_i} \,, \; T_G = \sum_{j=1}^{m} R_{G_j}. \tag{B2}$$

The Mann–Whitney statistic U is the number of pairs such that

$$U = \min \left(U_F, \; U_G \right), \tag{B3}$$

where $U_F = nm + \frac{n(n+1)}{2} - T_F$ and $U_G = nm + \frac{m(m+1)}{2} - T_G$.

The rejection of the null hypothesis is accomplished when p-value <0.05.